Oscillations of a standing shock wave generated by the Richtmyer-Meshkov instability

Karnig O. Mikaelian

Oscillations of a standing shock wave generated by the Richtmyer-Meshkov instability

Karnig O. Mikaelian

Lawrence Livermore National Laboratory, Livermore, California 94551, USA

In a typical Richtmyer-Meshkov experiment a fast moving flat shock strikes a stationary perturbed interface between fluids A and B creating a transmitted and a reflected shock, both of which are perturbed. We propose shock tube experiments in which the reflected shock is stationary in the laboratory. Such a standing perturbed shock undergoes well known damped oscillations. We present the conditions required for producing such a standing shock wave which greatly facilitates the measurement of the oscillations and their rate of damping. We define a critical density ratio $R^{critical}$ in terms of the adiabatic indices of the two fluids, and a critical Mach number $M_s^{critical}$ of the incident shock wave which produces a standing reflected wave. If the initial density ratio R of the two fluids is less than $R^{critical}$ then a standing shock wave is possible at $M_s = M_s^{critical}$. Otherwise a standing shock is not possible and the reflected wave always moves in the direction opposite the incident shock. Examples are given for present-day operating shock tubes with sinusoidal or inclined interfaces. We consider the effect of viscosity which affects the damping rate of the oscillations. We point out that nonlinear bubble and spike amplitudes depend relatively weakly on the viscosity of the fluids, and that the interface area is a better diagnostic.

I. INTRODUCTION AND GENERAL RESULTS

A most important and useful property of shocks is their stability. Undergoing damped oscillations, the first theoretical study of shock stability was by Roberts [1] followed by D'yakov [2], Freeman [3], and others – see Wouchuk *et al*. [4] and Bates [5] for an extensive list of references both old and new. Anomalous fluid properties, usually near a critical point, can lead to unstable shocks [2,6-8]. The influence of shock stability on inertial confinement fusion (ICF) has been assessed recently by 3D simulations [9].

In contrast, an interface between two fluids is unstable when impacted by a shock wave: the well-known Richtmyer-Meshkov (RM) instability [10,11]. The importance of the RM instability in ICF was pointed out some years ago [12] and since then it has been and continues to be studied extensively by theory [12-18], simulations [18-23], and experiments [24-31]. For a review see Refs. [32] and [33].

The stability of the shock wave and the instability of the interface are intimately connected by first publications [1,10] on each subject: Richtmyer's paper contains only one reference to prior work, and it is a reference to Roberts' report (there are no references in Roberts' report). Both were initially classified and subsequently declassified. Roberts' work is less known and referenced while Richtmyer's work continues to grow in readership. This could be due to two reasons: Roberts chose not to officially publish his work while Richtmyer did and, second, the stability of the shock wave attracts less attention than the instability of the interface which can lead to mixing between two fluids. Likewise, early experiments on shock stability were few and far in between [34,35] compared with the experiments on interface instability [11,24-31]. We

believe there is a third reason for the relative paucity of experiments on shock stability: Their relative difficulty arising from the fact that shocks, in general, move faster than interfaces. In this paper we propose a method to measure the oscillations of a standing shock, meaning a shock that is at rest in the laboratory frame.

Since traditionally the oscillations are detected by imaging techniques like schlieren and PLIF [34,35] (the same applies to the RM interface [11,24-31]), the advantages of imaging a standing shock versus a fast moving shock are obvious, a stationary object being much easier to image than a moving object. Another and, in our mind, a much more important advantage of a standing shock is that, in addition to standard imaging, experimentalists can use other diagnostic techniques when the target is at rest. In particular, a simple pressure gauge can record pressure oscillations as the standing shock oscillates back and forth around the fixed average location. We will illustrate with examples.

Interestingly, the method we propose uses the standard RM instability illustrated in Fig. 1 (This is the same as Fig. 1 of Ref. [15]. See also Fig. 1 of Ref. [10]): The incident shock, of Mach number M_s, travels "down" in fluid A and strikes the A/B interface, after which the interface begins to move down and its perturbations begin to grow (there are exceptions – see Ref. [15]). Ahead of the interface a transmitted shock also moves down in fluid B, while a reflected shock moves "up" in fluid A.

We use the same notation as in Ref. [15]: In Fig. 1 the velocity W_i of the incident shock, the jump velocity Δv of the interface, the velocity W_t of the transmitted shock, and the upward velocity W_r of the reflected shock are all taken to be positive. As we pointed out in Ref. [15], it is possible for the reflected shock to move down in the

laboratory frame, in which case W_r will turn out negative. Clearly, if W_r can be positive (moving up) or negative (moving down), it can also be zero, i.e., standing. It is this reflected shock, perturbed by the initial interface, that we propose to probe experimentally. When $W_r = 0$ the shock stays fixed where the interface was originally located, while the interface itself moves down and away from it.

A reader familiar with Ref. [35] will notice a similarity: Briscoe and Kovitz used a perturbed solid endwall to reflect an initially flat shock and measured the oscillations of the reflected shock as it moved up. We propose a perturbed *fluid*, instead of a solid endwall, that acts like a partial shock absorber and which, under the proper conditions, leaves behind a standing reflected shock while it (the absorber) moves away.

We know of only one experimental and one computational work studying the oscillations of one of the shocks in the RM instability. Both studies considered the *transmitted* shock. Aleshin *et al.* [36] studied the shock transmitted into Xe in a He/Xe or Ar/Xe system. Interpretation was rather difficult but decaying perturbations were observed on the transmitted shock front. The simulations [37] showed qualitative agreement with the experiment and went on to consider the air/SF_6 system, again focusing on the shock transmitted into the SF_6 (what we generically call gas B in the A/B system). We believe studying the *reflected* shock in gas A is more interesting because it can be made stationary.

Clearly, the proper conditions are obtained by setting $W_r = 0$. An expression for W_r was given in the Appendix of Ref. [15] (Eq. (A10)):

$$W_r = (u_3 \rho_3 / \rho_2 - u_2)/(1 - \rho_3 / \rho_2), \tag{1}$$

which follows from momentum conservation and is straightforward to derive, remembering that all parameters, in particular u_2 and u_3, refer to the laboratory frame. As is standard, in the reference frame of the shock the fluid velocities are $u_2 + W_r$ and $u_3 + W_r$, hence momentum conservation reads $\rho_2(u_2 + W_r) = \rho_3(u_3 + W_r)$, which gives Eq. (1) above. If $W_r = 0$ then $\rho_2 u_2 = \rho_3 u_3$, again a momentum-conservation equation because now the rest frame of the shock *is* the laboratory frame.

It turns out that $W_r = 0$ is allowed in most cases, *but not all cases*. In most cases, starting with a low Mach number M_s, the reflected shock moves up, i.e. $W_r > 0$ in our notation. As M_s and the downward fluid flow is increased W_r decreases, i.e. the reflected shock moves up less and less, as one would expect on physical grounds. At some special value of M_s, call it $M_s^{critical}$, the reflected shock becomes stationary, and this is the shock that we want. Any further increase in M_s is "overdrive" and the reflected shock moves down and W_r becomes negative. However, this does not happen in all cases – there are cases, as discussed below, that do not have an $M_s^{critical}$; In those cases W_r decreases as before but, before reaching zero, it reaches a minimum and then *increases* with increasing M_s. Although such cases are relatively rare, we hesitate calling them "anomalous" because we see nothing so out of the ordinary. For example we find that air/SF$_6$ admits $W_r = 0$, while He/air does not – As M_s increases its W_r has a minimum, approximately 50 cm/ms near $M_s \approx 5$, and then it climbs back up with increasing M_s. This is interesting because, as we have pointed out previously, air/SF$_6$ has approximately the same density ratio and hence the same Atwood number as the

He/air system and therefore the RM instability evolves similarly in both systems [38]. As before [15], we define $R \equiv \rho_B / \rho_A$ where $\rho_{A,B}$ are the initial, preshock densities of the fluids and define $A \equiv (R-1)/(R+1)$, also called A_{before} for the Atwood number before the shock.

We find that the existence or non-existence of $W_r = 0$ at finite M_s depends strongly on R and on the compressibilities of the fluids through their adiabatic indices γ_A and γ_B. Our results can be summarized by defining a critical density ratio $R^{critical}$:

$$R^{critical} \equiv \frac{(\gamma_A + 1)(3 - \gamma_A)}{(\gamma_B + 1)(\gamma_A - 1)^3} . \tag{2}$$

If the density ratio R of the system satisfies $R < R^{critical}$ then it does admit $W_r = 0$ and has an $M_s^{critical}$. If $R > R^{critical}$ then it does not admit $W_r = 0$ and has only a minimum $W_r > 0$. If $R = R^{critical}$ then the system admits $W_r = 0$ only at $M_s = \infty$. Eq. (2) is derived in the Appendix of this paper.

There is a second and perhaps more important motivation for the study of shock oscillations: Viscosity. Sakharov proposed measuring the viscosity of a fluid via its stabilizing effect on shock oscillations [39,40]. This well-known method is reviewed extensively by Miller and Ahrens [41] and interpretation of experiments continue to be contentious [42]. Of course viscosity has a stabilizing effect on the RM instability itself [43] and, recently, we proposed using that effect as an alternative to Sakharov's method [44]. By measuring *both* the oscillations of the shock and the evolution of the interface one is using both methods to extract viscosity. The importance of viscosity in ICF implosions has been recently studied by direct numerical simulations [45,46].

In summary, we are proposing RM experiments in which both the interface amplitude and the shock oscillations are measured simultaneously as functions of time. We believe this is possible only if $W_r = 0$. One first chooses a system with $R < R^{critical}$ and hence $W_r = 0$ is allowed. Next, one chooses that special Mach number $M_s^{critical}$ that actually produces $W_r = 0$, i.e. a standing reflected shock wave, which greatly facilitates probing it with imaging as well as static techniques. While probing the RM interface is challenging it has now been mastered by many groups [11,24-31]. Adding diagnostic to simultaneously measure the expected oscillations of the reflected shock may require new techniques, but we believe that that task is greatly simplified by choosing a standing wave.

In Sec. II we present several examples with and without a standing shock wave. In Sec. III we concentrate on a possible air/CO_2 experiment and present numerical simulations of the interface with the 2-dimensional hydrocode CALE [47]. In Sec. IV we study the oscillations of the standing reflected shock wave. In both of those sections (Secs. III and IV) we consider two types of interface perturbations: A) a sinusoidal interface and B) an inclined interface. While sinusoidal perturbations are by far the most common, inclined interfaces with no membranes have been recently produced [28,48]. The effect of a reshock generated by the solid endwall of the shock tube is taken up in Sec. V. In Sec. VI we briefly consider air/SF_6 experiments. Computational and other diagnostic techniques are discussed in Sec. VII, and concluding remarks are presented in Sec. VIII. In the Appendix we derive Eq. (2).

II. Standing Shocks

In the laboratory frame defined by $u_A = u_B = 0$ (see Fig. 1) the Mach number M_s specifies the wave velocity W_i of the incident shock and the material velocity u_3. As in Ref. [15] we take the downward direction as positive for all velocities except W_r, the velocity of the reflected shock, which is positive if moving "up." All postshock quantities like $\rho_{1,2}, u_{1,2}, p_{1,2}, W_r$ and W_t (velocity of the transmitted shock) can be found by using conservation of mass and momentum ("Hugoniot relations") across waves and the interface, a procedure that involves solving a transcendental equation (Eq. (A4) in Ref. [15]) which, in general, must be done numerically. It is clear, from physical considerations, that only W_r may be zero or negative - $u_{1,2,3}$ as well as W_t must be positive, i.e "down," a direction selected by the incident shock.

In Fig. 2 we plot W_r as a function of M_s for four systems: N_2/air, air/Xe, H_2/air, and He/air. As input we have taken densities $\rho_{A,B}$ and adiabatic indices $\gamma_{A,B}$ from Table I, following mostly Ref. [49]. One can easily verify that for the first three systems $R < R^{critical}$ and indeed their W_r curves cross the axis, i.e. $W_r = 0$, at $M_s^{critical} = 2.06$, 2.88, and 5.13 respectively. The fourth system, He/air, has $R > R^{critical}$ and it has only a rather wide minimum, $W_r \approx 50$ cm/ms near $M_s \approx 5$, after which W_r increases, albeit slowly, as shown in Fig. 2 and as we discussed in the previous section. As for other examples which do *not* admit $W_r = 0$ but have only a minimum we mention H_2/SF_6 and H_2/Xe, the latter presented as an example in the Appendix. In all cases $R^{critical}$ determines whether a pair

of gases admits $W_r = 0$ or not, i.e., whether a critical Mach number $M_s^{critical}$ exists or not: A standing shock can be found if and only if $R < R^{critical}$.

Two other systems are worth mentioning: air/SF$_6$ and air/CO$_2$, not shown in Fig. 2 so as not to crowd the curves. They have $M_s^{critical} = 2.76$ and 2.18 respectively. Air/SF$_6$ is extensively studied in shock tube experiments [24-31], while air/CO$_2$, somewhat less studied [31,50-52], will be considered in detail in the rest of this paper.

Let us compare and contrast the most commonly used system, air/SF$_6$, at $M_s = 1.20$ and at $M_s = M_s^{critical} = 2.76$. For the (almost standard) $M_s = 1.20$ case the incident shock wave moves down at $W_i \approx 400$ m/s. The interface, after being hit by that shock, moves down at a mere 70m/s while the transmitted shock moves ahead of it at $W_t \approx 175$ m/s, i.e. 2.5× faster. The reflected shock wave moves *up* about 4× faster at $W_r \approx 280$ m/s. If the experiment were done at $M_s = M_s^{critical} = 2.76$, one has $W_i \approx 950$ m/s, the interface after shock moves at a whopping 460 m/s, the transmitted shock a little faster at 500 m/s but, most importantly, the reflected shock is at rest, $W_r = 0$.

We next present the one-dimensional flow conditions for the air/CO$_2$ system whose two-dimensional behavior will be studied in subsequent sections at $M_s = M_s^{critical} = 2.18385$. As input we take p_0, the ambient pressure, to be atmospheric, $\rho_A = \rho_{air} = 1.205\,\text{Kg/m}^3$, $\rho_B = \rho_{CO_2} = 1.839\,\text{Kg/m}^3$, $\gamma_A = 1.402$, and $\gamma_B = 1.297$. The incident shock is traveling down at $W_i = 750\,\text{m/s}$. To complete the specification of the "before" state use standard relations [49] that give $p_3/p_0 = 5.40$, $\rho_3/\rho_A = 2.92$, and

$u_3 / c_A = 1.44$ ($c_A = 343 \, \text{m/s}$ is the sound speed in ambient air). Note that the flow within the singly-shocked air region #3 is slightly supersonic with $u_3 / c_3 \approx 1.058$.

As mentioned above, all "after" variables are easily obtained once Eq. (A4) in Ref. [15] is solved. We find $x = 1.138$. Using this value we find $\rho_1 / \rho_B = 3.50$, $\rho_2 / \rho_A = 3.21$, $p_1 / p_3 = p_2 / p_3 = 1.138$, $u_1 / c_B = 1.68$ ($c_B = \sqrt{\gamma_B p_0 / \rho_B} = 267 \, \text{m/s}$ is the sound speed in ambient CO_2), $W_t / c_B = 2.36$, which is the Mach number of the transmitted shock, and of course $W_r = 0$. This standing shock stands between the slightly supersonic singly-shocked air, i.e. region #3 where the pressure p_3 is 5.4× atmospheric, and the doubly shocked air, region #2, which is slightly subsonic with $u_2 / c_2 \approx 0.947$ and where the pressure is $1.138 \times 5.4 \times p_0$, i.e. slightly above 6 atmospheres. The jump velocity of the interface, commonly denoted by Δv, is given by $\Delta v = u_1 = u_2$ and is about 450 m/s, compared with 630 m/s $(= W_t)$ for the transmitted shock ahead of it. Needless to say, the fastest wave was the incident shock at $W_i = 750$ m/s.

III. AIR/CO$_2$: THE INTERFACE IN 2D

Having described the basic one-dimensional (1D) flow characteristics of the air /CO$_2$ system, we proceed to consider the evolution of perturbations at the interface using the two-dimensional (2D) hydrocode CALE [47]. As always, we first run the code in 1D mode to check that it indeed reproduces the 1D characteristics calculated analytically in the previous section.

We expect that such an experiment will measure both the interface and the reflected standing shock simultaneously. In this section we study the interface; the reflected shock

will be studied in the next section. We start with the interface first because this is by far the most common measurement of the RM instability.

As discussed in the Introduction we are interested in studying the effect viscosity has on perturbations appearing on the interface as well as on the shock. We believe such a shock tube experiment is an excellent venue to compare and contrast the two methods that have been proposed as a measure of viscosity: The RM method focusing on the interface [44] and the Sakharov method focusing on the shock [39-42]. For this purpose we will study four cases:

Case *A* (inviscid): $\mu_A = \mu_B = 0$, $\qquad\qquad\qquad\qquad\qquad\qquad$ (3a)

Case *B*: $\mu_A = 1\,\text{Pa.s}, \ \mu_B = 0$, $\qquad\qquad\qquad\qquad\qquad$ (3b)

Case *C*: $\mu_A = 0, \ \mu_B = 1\,\text{Pa.s}$, $\qquad\qquad\qquad\qquad\qquad$ (3c)

and

Case *D*: $\mu_A = \mu_B = 0.5\,\text{Pa.s}$, $\qquad\qquad\qquad\qquad\qquad$ (3d)

where μ_A and μ_B are the viscosities of fluids A and B, i.e. air and CO_2, respectively. The pros and cons of each method may be determined by how the perturbations respond to variations in viscosity.

We shall consider two types of perturbations as shown in Fig. 3: The standard sinusoidal perturbation (Fig. 3(a)) defined by amplitude η (initial value η_0) and wavelength λ, and the so-called inclined plane (Fig. 3(b)) defined by the shock tube width w and angle θ. The parameters in our simulations are taken to mimic experimental facilities [28,29] where such perturbations have been or can be produced. Specifically, $\lambda = 13\,\text{cm}$, $w = 11.43\,\text{cm}$, and $\theta = 60^o$. The sinusoidal perturbations are considered in subsection A and the inclined plane in subsection B.

A. Sinusoidal interface

The initial interface is taken to be $y = \eta_0 \cos kx$ with $k = 2\pi/\lambda$, $\lambda = 13$cm, and η_0 either small (3mm) or large (3cm). Bubbles, i.e., the penetration depth of the lighter fluid (air) into the heavier fluid (CO_2) are taken to be positive, while the spikes, i.e., the penetration depth of the heavier fluid into the lighter one, are taken to be negative. Referring to Fig. 3, the bubbles are at $x = 6.5$ and 19.5 cm, while the spikes are at $x = 0$, 13, and 26cm. It is well known that in the linear regime where $\eta k \ll 1$ bubbles and spikes are equal in magnitude but they are different in the nonlinear regime.

Fig 4 shows the evolution of the bubble and spike amplitudes starting with the small initial amplitude $\eta_0 = 3$mm. As usual, one defines $t = 0$ as the time the incident $M_s = 2.18$ shock in air strikes the interface. The amplitude is first compressed and then grows with time. The compression factor, as given by Richtmyer [10], is $1 - \Delta v/W_i \approx 1 - 450/750 \approx 0.4$. As expected the inviscid (red) case grows largest; the viscous cases (Eqs. 3b, 3c, and 3d) grow less, but all three cases are similar to each other. This is due to the choice $\mu_A + \mu_B = 1$pa.s in all three cases and the observation that the evolution of $\eta(t)$ depends primarily on the sum of the two viscosities [44]. This will not be true for the reflected shock, as will be discussed in Sec. IV. We should point out that 1pa.s is a greatly and artificially enhanced viscosity for air or CO_2 done numerically to more clearly interrogate the effect of viscosity on the interface and on the reflected shock.

During the 4ms shown in Fig. 4 the interface moves $450 \times 4/1000 \approx 1.8$m, while the initial 3mm perturbations grow to at most 2.6cm (inviscid spike in Fig. 4) for a growth

factor η/η_0 of about 9. This calls for a long shock tube. The total length L of the test section containing CO_2 is determined not by the distance the interface moves but by the requirement that the much-faster-moving transmitted shock (630m/s) does not hit the endwall and return to reshock the interface. One can easily show that $L \approx 250\,cm$ is sufficient to avoid a reshock before 4ms. A much shorter test section, $L = 50\,cm$, with reshock will be considered in Sec. V.

Keeping everything the same we increase the initial amplitude tenfold to $\eta_0 = 3\,cm$. The result is shown in Fig. 5. The amplitude again compresses by a factor of 0.4, but the subsequent evolution is quite different from the previous low-amplitude run: The inviscid case, case *A*, no longer dominates over the viscous cases *B*, *C*, and *D*. After growing for about 1ms the bubble begins to *decrease* and in fact is the smallest of all the bubbles after another millisecond. By 4ms the largest spike is case *C*, in blue in Fig. 5, reaching about 9cm in magnitude for a growth factor of 3; The smallest spike is case *B*, in black, at about 7cm, while cases *A* and *D*, red and grey respectively, are about equal at about 8cm.

We believe this is the first report of a viscous instability growing larger than the inviscid case. It appears to be the result of combining three properties: nonlinearity, compressibility, and low Atwood number ($A_{before} \approx 0.21$, $A_{after} \approx 0.25$). Unlike the linear case shown in Fig. 4 where the inviscid growth dominates, here viscosity appears to have little effect. This is, however, somewhat deceptive because the inviscid case supports a large amount of roll-up while the viscous cases do not. Fig.6 shows the air/CO_2 interface at the end of the runs, 4ms, for the 4 cases. Although penetration depths, i.e., bubbles and spikes, are comparable for the 4 cases, the inviscid case (Fig. 6(a)) does not dominate

precisely because it rolls up instead of growing vertically. As far as we can determine it is the same roll-up of the spike that causes its bubble to slow down and reverse curvature.

Comparing the (semi)linear case Fig. 4 with the nonlinear case Fig. 5 we clearly see how viscosity has a weaker effect in nonlinear problems, as reported in Ref. [44], and how the sum $\mu_A + \mu_B$, rather that individual viscosities μ_A and μ_B, that is the primary parameter with the 3 viscous cases B, C, and D yielding similar bubbles and spikes (Fig. 5) and configurations (Fig. 6).

B. Inclined interface

From the 26cm-wide shock tube [25,50-51] with a sinusoidal perturbation (Fig. 3(a)) we turn to an 11.43cm-wide shock tube [28,52] with an inclined interface (Fig. 3(b)). Instead of $y = \eta_0 \cos kx$ the interface is now linear in x and given by

$$y = (w/2 - x)/\tan\theta = \eta_0 - x/\tan\theta , \ 0 \le x \le w, \tag{4}$$

where

$$\eta_0 \equiv w/2\tan\theta . \tag{5}$$

For $w = 11.43\,\mathrm{cm}$ and $\theta = 60^o$ we have $\eta_0 \approx 3.3\,\mathrm{cm}$.

Since the walls of the shock tube are reflecting, the inclined interface can be considered as half of a "V" pattern $2w$ wide. As shown in Ref. [53] a "V" pattern can be Fourier expanded (Eq. (4b) in Ref. [53]) and the fundamental mode carries the lion's share of the expansion, $8/\pi^2$, or about 81%. The remaining infinitely many components of shorter and shorter wavelengths make up the remaining 19%. Hence to a good approximation the initial interface of Fig. 3(b) can be considered half of a sinusoidal

perturbation, $\eta_0 \cos(2\pi x/\lambda)$, $0 \le x \le \lambda/2$ having wavelength $\lambda = 2w = 22.86\,\text{cm}$ and amplitude $\eta_0 = w/2\tan\theta \approx 3.3\,\text{cm}$. In this approximation the width of the shock tube determines the wavelength of the perturbation and θ, the angle between the wall of the shock tube and the interface, determines the initial amplitude: Small amplitudes for $\theta \approx \pi/2$, large amplitudes for $\theta \approx 0$. In the laboratory the A/B fluid interface is horizontal and the shock tube is tilted at an angle $\pi/2 - \theta$ with the vertical [28,52].

Given the above mapping $(w,\theta) \to (\lambda,\eta_0) = (2w, w/2\tan\theta)$ it is not surprising that our simulations of this inclined interface yield results qualitatively similar to the large-η_0 (3cm) case in the previous subsection. We again simulate a flat shock falling on an inclined air/CO_2 interface leaving behind a standing shock, $M_s = 2.18385$. The evolution of the bubble and spike is shown in Fig. 7 which, as anticipated, is similar to Fig. 5 for a sinusoidal interface. In both figures viscosity plays a relatively small role because the initial amplitude, ~3cm, is large in both cases. In Sec. VI we discuss another diagnostic, interface area, which is much more sensitive to viscosity.

Fig. 8 shows the interfaces for the 4 inviscid/viscous cases as defined by Eqs. (3a)-(3d). The inviscid case, Fig. 8(a), shows much roll-up, the viscous cases, Figs. 8(b)-8(d), practically none. Qualitatively, these results are similar to Fig. 6 and support the identification of an inclined plane with half of a full wavelength.

In addition to $\theta = 60^o$ we carried out simulations with $\theta = 87^o$, i.e., a 3° tilt, for which $w/2\tan\theta \approx 0.3\,\text{cm}$, about 10× smaller than the 30° tilt. The resulting bubbles and spikes were similar to our earlier sinusoidal simulations with $\eta_0 = 0.3\,\text{cm}$ shown in Fig. 4

and, as in that figure, viscosity played a greater role and the inviscid amplitude grew larger than the viscous ones, as is normal.

IV. AIR/CO$_2$: THE REFLECTED, STANDING SHOCK IN 2D

To solve for the interface evolution one must solve simultaneously for all 3 "after" perturbed quantities: The interface, the transmitted shock, and the reflected shock. Given the initial ("before") perturbation amplitude $\eta_0 \equiv \eta_{0-}$ on the interface, Richtmyer [10] gave expressions for the perturbation amplitudes on all 3 of them immediately "after," $t = 0+$:

$$\eta_{0+}^{\text{interface}} = \eta_0(1 - \Delta v / W_i), \tag{6}$$

$$\eta_{0+}^{\text{trans.shock}} = \eta_0(1 - W_t / W_i), \tag{7}$$

and

$$\eta_{0+}^{\text{refl.shock}} = \eta_0(1 + W_r / W_i). \tag{8}$$

From Eq. (8) it follows that if $W_r = 0$ then the reflected shock not only stays at the location of the "before" interface but also acquires the same amplitude η_0.

To emphasize the requirement of simultaneity we remind the reader that the *same* CALE calculations which gave the interface evolution presented in the preceding section are used here to present the oscillations of the reflected shock just as, we hope, the same experiment will capture the interface as well as the reflected shock. It is somewhat ironic that the interface, despite the past vast experience with it, will probably prove to be the

more challenging measurement because of its large speed (450m/s), compared with the reflected shock which is at rest, on average, in the laboratory.

A. Sinusoidal interface

For brevity we shall consider only the large amplitude, $\eta_0 = 3$cm, case. As diagnostic, perhaps measurement with pressure transducers, either on the wall of the shock tube or within the flow, is the simplest method, followed by imaging − See below. Two such possible locations are indicated in Fig. 3(a): In the calculations we placed several tracer particles (only two are shown in Figs. 3(a) and 3(b)) which are fixed in position and which monitor flow parameters like density, pressure, temperature, etc. Their locations in Fig. 3(a) are $(x, y) = (0,$-6$)$ and (6.5, -6) in cm, in laboratory coordinates where the original perturbed interface, of wavelength 13 cm, lies between $y = +3$cm and -3cm.

As we saw in Sec. II, $p_3 \approx 5.40$ b and $p_2 \approx 6.15$ b (we set $p_0 = 1$ b), meaning the reflected shock sits between air at pressure ≈ 5.4 b (above) and 6.15 b (below). These are averages, i.e., one-dimensional values − The pressure fluctuates substantially, as expected. In Fig. 9 we plot the pressure difference Δp between the two points shown in Fig. 3(a) as a function of time. For clarity the viscous cases **B**, **C**, and **D** are displaced by -1, -2, and -3 units respectively. We see that the maximum Δp's are about ½ b, decreasing with time, particularly for cases **B** and **D**. For each case Fig. 6 showed the interface which, at 4ms, is about 180 cm below its original ($y = 0$) location.

From Fig. 9 it is clear that, unlike the interface whose evolution is controlled primarily by the sum $\mu_A + \mu_B$, the reflected shock probes primarily μ_A (A=air), which is not surprising because the reflected shock resides in fluid A. There is some difference between cases **A** and **C**, which differ only by the viscosity of the CO_2, but this difference is small and probably undetectable. The similarity of cases **B** and **D** also speaks for μ_B being a minor player in the behavior of the reflected shock. The difference here is primarily due to μ_A=1Pa.s in case **B** versus μ_A=0.5Pa.s in case **D**, the smaller viscosity leading to slightly larger and longer-lasting oscillation.

The density fields for cases **A** and **D** at t=1ms and 2ms are shown in Fig. 10. The pressure fields (not shown) are similar. In both cases the configurations, as indicated by the color maps, are quite different between the two times, but of course for case **D** the contrast is less and almost gone by 2ms – see the grey curve in Fig. 9.

B. Inclined interface

We now turn to the inclined interface shown in Fig. 3(b) and repeat the above procedure, i.e., extract the pressure oscillations in the reflected, stationary shock from the same calculation that gave the behavior of the interface (Fig. 7 and 8) as it recedes from its original location.

Fig. 11 shows the pressure difference, as a function of time, between the two stationary points indicated in Fig. 3(b) and whose coordinates are $(x,y) = (0,-4)$ and $(11.43,-4)$ in cm, i.e. both points are on the walls of the shock tube and 4cm below the initial interface. As in the sinusoidal case we have chosen points below the interface and hence in the initial CO_2 because we believe it will not be practical to position detectors on

the interface itself which would be optimal. Of course once the CO_2 is swept away by the incoming shock those fixed points remain in air and are just below the standing shock.

Our discussion of Fig. 9 applies to Fig. 11 also and will not be repeated. Snapshots of the *A* and *D* cases at 1 and 2 ms are given in Fig. 12 to be compared with Fig. 10.

V. RESHOCKED INTERFACE

As mentioned in the previous section a long, $L \approx 250\,\text{cm}$ shock tube is needed to observe the interface for 4ms without a reshock. In this section we consider a much shorter, $L = 50\,\text{cm}$ test section in which the interface is reshocked a mere 1ms after the incident shock, i.e., after travelling only 45 cm. We will compare the evolution of the interface between the long and short test sections for cases **A** and **D**.

Starting with the inviscid case *A* and the large ($\eta_0 = 3\,\text{cm}$) initial amplitude, Fig. 13 compares the evolution of the reshocked interface with the previous unreshocked interface. Needless to say, until 1ms the two evolve identically. At 1ms, Fig. 13 shows the bubbles, or the lower part of the interface, flattened by the reshock in the short-test-section case. The spikes are still identical because the reshock has not yet reached them.

By 1.3ms the reshock has cleared the spikes also and the whole interface is now compressed and highly complex after the reshock, while the unreshocked case evolves freely with its spikes wrapping ever more tightly with time (its configuration at 4ms was

shown in Fig. 6(a)). Because it was moving from the heavy (CO_2) into the light fluid (air), by 2ms the reshock has inverted the interface as expected and as seen in Fig. 13.

The same comparison between long and short test sections for the viscous case **D** is presented in Fig. 14. Because the fluids are assumed to be viscous the evolution is slower and the inverted interface at $t = 2$ms is less convoluted than in Fig. 13, but otherwise the processes are totally similar.

We should point out that for the unreshocked case (left columns in Fig. 13 and 14) the interface is moving down at about 450m/s, but in the reshocked case (right columns) the interface is practically at rest about 5cm above the endwall, i. e. 45cm below its original location, so that in Fig. 13 and 14 the snapshots in the left and right columns are at the same *times* but certainly not at the same positions, except for $t = 1$ms.

VI. AIR/SF$_6$

In this section we discuss possible air/SF_6 experiments at $M_s = M_s^{critical} = 2.76$. The 1D properties of this flow were already presented in Sec. II. Here, for brevity, we concentrate on the sinusoidal interface with $\lambda = 13$ cm and $\eta_0 = 1$ cm.

SF_6 is heavier than CO_2 and more compressible (see Table 1.) Consequently the Atwood number is higher and perturbations at the air/SF_6 interface grow faster than in air/CO_2. It is interesting, though more of a coincidence, that the interfaces in the two cases move at almost the same speed: 45 cm/ms for air/CO_2 at $M_s = 2.18$ and 46 cm/ms for air/SF_6 at $M_s = 2.76$. The reason is that the higher density of SF_6 counterbalances the higher Mach number leading to almost the same Δv.

The main consequence of the low value of γ_{SF_6}, 1.090 compared with CO_2's 1.297, is that the transmitted shock is slow: 50 cm/ms compared with CO_2's 63 cm/ms. This implies that the transmitted shock takes a very long time to separate from the interface, similar to the He/Freon-22 case discussed in [15]. In Fig. 15 we compare air/SF_6 with air/CO_2. In air/SF_6 the transmitted shock is seen in all of the frames while in air/CO_2 it is seen only in the first frame, at $t = 0.5$ ms, being too far away to be captured in the rest of the frames. At $t = 2$ ms, for example, the transmitted shock in air/SF_6 is only 8 cm away from the interface $(2\times(50\text{-}46)\text{=}8)$, while it is $2\times(63\text{-}45)\text{=}36$ cm below the air/CO_2 interface.

Snapshots of the density configuration taken at different times but at the same location of the standing shock are shown in Fig. 16. As in Fig. 10 the coordinates of the four corners are (0,-30), (26,-30), (26,-4), and (0,-4) in cm, and of course the "camera" frame is *fixed* in space – the great advantage of a standing shock.

In Fig. 17 we display what we believe is the simplest diagnostic of all, the pressure difference between two pressure gauges located at the two points indicated in Fig. 3a. The average pressure p_2 is about 15.4 bars, varying between 14.6 and 16.3 bars at those two points. From Fig. 17 it is clear that the pressure oscillations are decreasing with time, just as the original [1] calculations indicated, albeit for an isolated shock.

We should add that a similar behavior is seen if, instead of pressure, one monitors the temperature: The average value is 830K, and varies between 825K and 845K and, like the pressure shown in Fig. 17, the oscillations decrease with time.

We have repeated all of the above inviscid calculations with excessively large values, 0.5-1.0 Pa.s, for μ_A or μ_B as listed under cases **B**, **C**, and **D** in Eqs. (3b), (3c), and (3d).

As expected, the results are similar to the air/CO$_2$ experiment discussed at length in previous sections: Viscosity slows down the growth of short-wavelength perturbations and causes the oscillations in a perturbed shock to decay faster.

We emphasize that such large values for $\mu_{A,B}$ were chosen only to illustrate the effect of viscosity and do not represent the actual viscosities of gases which are smaller by about 5 orders of magnitude. For example [54], $\mu_0(\text{air}) \approx 1.8\text{e-5}$ Pa.s, $\mu_0(\text{CO}_2) \approx \mu_0(\text{SF}_6) \approx 1.5\text{e-5}$ Pa.s, the subscript 0 denoting ambient conditions. The temperatures of the shocked gases increase by factors of 2-3, as given by $T_i/T_0 = (p_i \rho_0)/(p_0 \rho_i)$. In this regime viscosity also increases with temperature and can be estimated either by consulting tables or by using Sutherland's law [54]. We find that postshock temperatures for the various gases lie between 480 K and 830 K and the increased physical viscosities range from 2.3e-5 Pa.s to 3.8e-5 Pa.s. We repeated our air/CO$_2$ and air/SF$_6$ simulations with $\mu_A = \mu_B = 5\text{e-5}$ Pa.s, a generous estimate for the viscosities. The results could hardly be distinguished from the inviscid calculations.

VII. COMPUTATIONAL METHODS AND DIAGNOSTICS

As Richtmyer pointed out the shocks are not isolated but communicate with the interface. This presented particular challenges to solving even the linearized problem numerically [10]. Our numerical simulations, which are fully nonlinear solving the Navier-Stokes equations on a grid, presented a challenge we had not encountered previously.

CALE is an ALE (arbitrary Lagrangian-Eulerian) code [47] ideally suited to track the distortions of an interface. One uses a fine conformal grid to capture the initial interface, and a coarser resolution away from the interface is usually sufficient to capture the before and after shocks. The high-resolution ALE mesh moves mostly with the interface and sustains the developing "mushrooms" on it. We used this approach in all our previous simulations which focused on the interface only. For the present problem, however, this method gives too poor a resolution for the shocks whose oscillations we wish to study. Clearly, ALE methods coupled with AMR (Adaptive Mesh Refinement) techniques [55] would be ideal as one could then resolve *both* the interface as well as the shocks at different distinct locations, but CALE does not have AMR capability.

We tried an alternative approach: Running Eulerian, i.e., the grid stays fixed as material flows though it, with the mesh again highly resolved near the interface and tapering away from it. Since the reflected shock stays at the location of the original interface (when $W_r = 0$), it remains in the highly-resolved area. But now the interface was poorly resolved as it moved away. Our final choice was to run Eulerian with a fine grid throughout the whole problem at the price of increasing the computational cost.

Most of our final Eulerian simulations had a grid spacing of 2mm and 0.46mm in the horizontal and vertical directions respectively. As a check, we compared the interface evolution with the ALE simulation mentioned above and which resolved, as usual, the interface quite well; We found good agreement. We also compared the reflected shock with the Eulerian simulation mentioned above and which resolved the standing shock quite well; again we found good agreement. Since the interface and the shocks communicate with each other, and for aesthetic reasons, we chose not to present

interfaces from one calculation (ALE) and shocks from another (Eulerian resolved near the interface), but to present both from a single calculation (Eulerian resolved everywhere) as of course the experiment would be. We repeat that AMR would have been much more efficient at providing resolution where it is needed [55].

Fig. 18 compares the above mentioned calculation with one where the grid is finer: 0.5mm by 0.23mm. We ran this finer-zoned problem to 1.12ms. The "mushrooms" are more tightly wound in the higher-resolution problem but generally agree with the lower-resolution run, as does the Δp signal.

We take this opportunity to discuss another metric, the interface area A_I, proposed by Renoult *et al*. [56] and Kilchyk *et al*. [57] as a diagnostic for instability growth, in addition to the usual bubble and spike amplitudes. We have used this metric to discuss the Boussinesq approximation to RT and RM instabilities [58]. Returning to Figs. 5 and 7 above, we see that in the nonlinear regime bubbles and spikes can be comparable for viscous and inviscid cases *A* through *D*, but interface *shapes* can easily distinguish them, as can be seen in Figs. 6 and 8. Obviously, the interface area A_I is a much better measure of interface shape than just bubble/spike amplitudes. In Figs. 6 and 8 the inviscid case *A*, having highly evolved mushrooms, is quite different from and has the much higher interface area A_I than cases *B-D*, all viscous. Indeed A_I is a useful diagnostic in addition to $\eta^{b,s}$.

In 2D planar problems A_I is a constant multiple of L_I, the arclength of the interface, and can be calculated by CALE. However a cut-off filter corresponding to experimental resolution must be used to make meaningful statements concerning A_I because it is poorly defined for inviscid problems and can be a strong function of the numerical

resolution used to calculate it. For example, in Fig. 18, our standard resolution gives $L_I \approx 50$ cm (per each wavelength) but the higher-resolution gives ≈ 70cm, the extra 20cm coming from the more tightly wound vortices in the mushroom. It follows that interface areas A_I or lengths L_I must be compared at the same resolution, which we do using our standard 2mm$\times$0.46mm grid.

Fig. 19 shows the excess area ratio (defined below) for the sinusoidal interface, $\lambda = 13$cm, $\eta_0 = 3$cm, and for the inclined interface, $w = 11.43$cm, $\theta = 60°$, in each geometry using red for the inviscid case A and grey for the viscous case D. Note the large difference viscosity makes, resulting in factors of 4-5. Compare with Fig. 5 (sinusoidal) and Fig. 7 (inclined) where viscosity hardly made a difference for the bubbles or the spikes (However, linear amplitudes do discriminate – see Fig. 4). The more graphic comparison was seen in Figs. 6 and 8 where all diagrams have approximately the same overall height but the inviscid case (Fig. 6(a) and 8(a)) have much larger interface areas. For example, $L_I \approx 180$cm in Fig. 6(a), almost 4$\times$ longer than $L_I \approx 48$cm in Fig. 6(d), because of viscosity.

The excess area ratio is defined as [58]

$$E(t) \equiv \frac{A_I(\eta)}{A_I(0)} - 1 = \frac{L_I(\eta)}{\lambda} - 1, \tag{9}$$

the second equality holding for 2D, where L_I is the interface length per each wavelength. The initial values $E(0)$ can be calculated analytically and we start with the inclined plane because it is the simplest interface. From Fig. 3(b) $\sin\theta = w/L_I(0)$, hence

$$E_{inclined} = \csc\theta - 1. \tag{10}$$

For $\theta = 60^\circ$ we get $E_{inclined}(0) = 2/\sqrt{3} - 1 \approx 0.15$. This agrees with the initial, preshock values seen in the simulations of Fig. 19. Note that this is the same value for a full "V" shape where both w and L_I are multiplied by 2 leaving Eq. (10) unchanged.

For a sinusoidal interface $y = \eta_0 \cos kx$ and we have

$$L_I(0) = \int \sqrt{1 + \left(\frac{dy}{dx}\right)^2} dx = \int_0^\lambda \sqrt{1 + (\eta_0 k)^2 \sin^2 kx} \, dx = \frac{4}{k} \int_0^{\pi/2} \sqrt{1 + (\eta_0 k)^2 \sin^2 \alpha} \, d\alpha. \tag{11}$$

From Ref. [59],

$$\int_0^{\pi/2} \sqrt{1 + p^2 \sin^2 \alpha} \, d\alpha = \sqrt{1 + p^2} \, I\left(\frac{p}{\sqrt{1 + p^2}}\right) \tag{12}$$

where I is the widely tabulated [60] complete elliptic function

$$I(\kappa) \equiv \int_0^{\pi/2} \sqrt{1 - \kappa^2 \sin^2 \alpha} \, d\alpha. \tag{13}$$

Combining Eqs. (11)-(13) we get

$$E_{sinusoidal} = L_I / \lambda - 1 = \frac{2}{\pi} \sqrt{1 + (\eta_0 k)^2} \, I\left(\frac{\eta_0 k}{\sqrt{1 + (\eta_0 k)^2}}\right) - 1 \ . \tag{14}$$

For $0 \leq \kappa \leq 1$ $I(\kappa)$ varies between $\pi/2$ and 1.

For small $\eta_0 k$ Eq. (14) can be expanded and we find:

$$E_{sinusoidal} \approx (\eta_0 k)^2 / 4 \, , \ \eta_0 k \ll 1 \ . \tag{15}$$

The above approximation can be used for our small-η_0, $\eta_0 = 0.3$cm calculation for which $\eta_0 k = 0.145$ and we find $E \approx 5.26\text{e-}3$. For large $\eta_0 k \approx 1.45$ as in our $\eta_0 = 3$cm run, tables must be consulted [60] and we find $\eta_0 k / \sqrt{1 + (\eta_0 k)^2} \approx 0.82$, $I(0.82) \approx 1.25$, and $E \approx 0.40$, which agrees with the initial, preshock value shown in Fig. 19.

As Fig. 19 shows, the excess values before the shock, $E_{\text{inclined}}(0-) \approx 0.15$ and $E_{\text{sinusoidal}}(0-) \approx 0.40$, get substantially compressed by the shock and then grow. The compressed values, denoted by $E(0+)$, can be calculated the same way as above, using Richtmyer's compression factor $1 - \Delta v / W_i \approx 1/2.5$ for η_0 (see Eq. (6)). For the inclined plane compression by a factor of 2.5 increases θ_{before} from 60° to $\theta_{after} \approx 77^o$, hence $E_{\text{inclined}}(0+) \approx \csc 77^o - 1 \approx 0.026$, a sixfold drop from $E_{\text{inclined}}(0-) \approx 0.15$. Again, our simulations (Fig. 19) show this to be correct. For the sinusoidal case, $(\eta_0 k)_{after} = (\eta_0 k)_{before} / 2.5 = 1.45 / 2.5 = 0.58$, $\eta_0 k / \sqrt{1 + (\eta_0 k)^2} \approx 0.50$, $I(0.50) \approx 1.47$, hence $E_{\text{sinusoidal}}(0+) \approx 0.082$, approximately fivefold decrease from $E_{\text{sinusoidal}}(0-) \approx 0.40$, again in agreement with the simulations in Fig. 19. Thus when η_0 compresses by a factor 2.5 the excess area ratios E decrease by factors of 5-6 showing that interface area (or arclength) is more sensitive to compression. For other shapes one can approximate $E \sim (\eta_0 k)^2$ in the linear regime, hence E compresses by the factor $(1 - \Delta v / W_i)^2$ for any shape in this regime: when the amplitude compresses 2.5 times E compresses by $(2.5)^2 = 6.25$.

VIII. REMARKS AND CONCLUSIONS

In this paper we have proposed RM experiments in which both the interface *and* the reflected shock are investigated, simultaneously, as opposed to the standard operation of measuring the interface only in an RM experiment. By choosing $M_s = M_s^{critical}$ the reflected shock is stationary in the laboratory at the original location of the interface and this, we believe, will greatly facilitate the analysis of its decaying oscillations. As

expected, viscosity damps the oscillations even more, and we illustrated with the air/CO_2 system having a sinusoidal or an inclined interface.

We conclude with a few remarks:

1) The air/CO_2 experiment discussed in this paper has relatively modest requirements. In addition to generating the $M_s = 2.18$ shock in air the shock tube must contain the shocked CO_2 in which the transmitted shock is moving at $M_t = 2.36$ - see the discussion in Sec. II. From Fig. 1 it is clear that, in general, the highest pressures are encountered in the test section, i.e. $p_1 (= p_2)$. For the air/CO_2 system $p_1 / p_0 \approx 6.1$, meaning the test section must withstand at least 6.1 atmospheres if $p_0 \approx 1$ atmosphere. Air/Ar is another system with properties similar to air/CO_2 and hence easily accessible.

Air/SF_6, the other system discussed in Sec. II and in Sec. VI, requires slightly higher M_s, about 2.76, to produce a standing shock, but a considerably stronger, structurally, shock tube because the transmitted shock, moving at about 500m/s, has $M_t \equiv W_t / c_B \approx 500 / 134 \approx 3.73$, where $c_B \approx 134$ m/s is the very low sound speed in ambient SF_6. In terms of pressure, $p_1 / p_0 \approx 15.4$, more than twice the 6.1 needed for CO_2. Slightly higher containment is required for air/Xe: 17.8. As to H_2/air, which requires $M_s = M_s^{critical} \approx 5.13$ to produce a standing shock (see Fig. 2), it generates a very high $p_1 / p_0 \approx 93.0$.

However, we must point out that a common technique to produce and contain high-Mach-number shocks is to partially evacuate the shock tube. For example, Vetter and Sturtevant [25] carried out experiments at ~1/4 atmosphere ($p_0 = 23$

kPa) in which case the p_1 values would decrease proportionately to 1.5, 3.9, 4.5 and 23.3 atmospheres for air/CO_2, air/SF_6, air/Xe and H_2/air, respectively.

2) We urge experimentalists to re-assess the utility of using thin membranes to separate fluids A and B, whatever they are. Using membranes one can easily set up initial interfaces of arbitrary shapes. Many experiments have already used thin membranes [11,25-27,36,48,50,63] or soap [29,61-62]. Eretz *et al.* [63] found membranes to have little effect on large, single-scale perturbations. Ideally, one would like to avoid the use of membranes as they complicate somewhat the analysis of the experiments and their numerical simulation. Several membraneless experiments have been reported [24,28,30-31,51-52,56]. However, a highly complex procedure is required to generate a membraneless interface, it is usually not sharp but diffuse, and of course one can impose only limited shapes on membraneless interfaces.

3) There are advantages and disadvantages for each of the two techniques discussed so far that measure viscosity at high pressure, viz. damping of shock oscillations [39-41] (Sakharov's method) or damping of the RM interface growth [44]. The advantage of the first, Sakharov's method, is that the damping depends primarily on μ_A, the viscosity of the fluid in which the shock is moving (or is "at rest"). In contrast, the second, RM-interface method, is sensitive to the sum $\mu_A + \mu_B$, which is a disadvantage. As we have shown in this paper one can choose conditions whereby the reflected shock is stationary thus greatly facilitating its observation. For a given pair of fluids A and B this can be done at only one specific Mach number, $M_s = M_s^{critical}$, which is a limitation. However, by changing fluid B one

can study shock oscillations at different Mach numbers or pressures. In the air/CO_2 example chosen in the present work the standing shock was produced in air at $M_s = M_s^{critical} \approx 2.18$, the pressure on either side of the shock varying between 5.4b and 6.1b. Thinking of fluid B as a "shock absorber/reflector," one can replace the CO_2 by Xe and, as can be seen in Fig. 2, one again has a standing shock in air but now at $M_s = M_s^{critical} \approx 2.88$, with pressures of 9.5b and 17.8b on either side of the shock. Let us point out that if M_s is not exactly at $M_s^{critical}$ but slightly above or below it, then the reflected shock will slowly drift down ($W_r < 0$) or up ($W_r > 0$).

The second method, measuring the interface behavior, is not limited to one Mach number, which is an advantage. Needless to say, the method that we have proposed in this paper, viz. measuring *both* the interface behavior as well as the shock oscillations simultaneously, provides more data on μ_A and $\mu_A + \mu_B$ and can be thought of as two experiments in one.

4) For the interface technique we have seen that the interface area is more sensitive to viscosity than the more commonly measured quantities η^b or η^s. For 2D inclined and sinusoidal interfaces we gave Eqs. (10) and (14), respectively, measuring effectively the arclength of the initial interface. Those expressions are not limited to the linear regime and can be applied (and even simplified) for steep inclines or large amplitudes. For example, for very *large* $\eta_0 k$ we have $I \to I(1) = 1$ and Eq. (14) reduces to $E \to 2\eta_0 k / \pi = 4\eta_0 / \lambda$. However, Eqs. (10) and (14) apply only to those two shapes. In the future we hope to pursue

analytically or semi-analytically other shapes more representative of the nonlinear evolution in RT and RM instabilities. A study of different shapes in the RM instability was initiated in Ref. [64] and recent simulations track how different shapes evolve into liquid jets [65].

5) Finally, we hope to explore the behavior of perturbed shocks in solid state materials with strength. With the proper choice of material B as the shock absorber/reflector, it should be straightforward to generate a standing shock in material A. If A does not melt and retains some of its strength we again expect perturbations to damp out as a result of material strength. We have proposed a correspondence between strength and viscosity (Eq. (6) in Ref. [44]) that governs, approximately, the behavior of perturbations at a shocked solid interface. Whether a similar correspondence exists for perturbed shocks remains to be seen in future investigations, both calculational and experimental.

APPENDIX: $R^{critical}$

The critical density ratio $R^{critical}$ given in Eq. (2) is derived by requiring that the reflected shock wave be standing ($W_r = 0$) when $M_s = \infty$.

As discussed in Ref. [15], the basic flow for the RM instability is specified by the 6 properties of the system: ρ_A, ρ_B, γ_A, γ_B, p_0, and p_3 - See Fig. 1. These variables can be reduced to 4 by working only with nondimensional quantities which can be taken as $R \equiv \rho_B / \rho_A$, γ_A, γ_B, and M_s. Other "before" quantities such as ρ_3, u_3, etc. can be obtained in a straightforward manner. "After" quantities like $\rho_{1,2}$, $u_{1,2}$, etc. can be found once a transcendental equation, Eq. (A4) in Ref. [15], is solved and $x \equiv p_2 / p_3$ is at hand. Since we are focusing on the case where a shock is reflected, $x > 1$. All the curves in Fig. 2 and Fig. 20 below are obtained in this manner.

Fortunately, that transcendental equation is somewhat simplified by going to the strong shock limit: Eq. (A15) of Ref. [15] reads

$$[x(\gamma_A + 1)/R(\gamma_B + 1)]^{1/2} = 1 + \frac{1 - x}{[1 + mx]^{1/2}} \tag{A1}$$

where $m \equiv (\gamma_A + 1)/(\gamma_A - 1)$. This is our first condition. Our second condition is that $W_r = 0$ and hence $u_3 \rho_3 = u_2 \rho_2$ as discussed in the Introduction. The strong shock limit of the four variables $u_{2,3}$ and $\rho_{2,3}$ are obtained from Eqs. (A1), (A2), (A6), and (A8) of Ref. [15] by letting $p_3 / p_0 \rightarrow \infty$ and we find:

$$\rho_3 / \rho_A = \frac{\gamma_A + 1}{\gamma_A - 1} = m, \tag{A2}$$

$$u_3^2 = \frac{2 p_3}{\rho_A(\gamma_A + 1)}, \tag{A3}$$

$$\rho_2 / \rho_A = (\gamma_A + 1)[x(\gamma_A + 1) + \gamma_A - 1]/(\gamma_A - 1)[x(\gamma_A - 1) + \gamma_A + 1]$$
$$= m[mx + 1]/[x + m], \tag{A4}$$

and

$$u_2^2 = 2xp_3 / \rho_B(\gamma_B + 1).$$ (A5)

Substituting the above equations in $u_3\rho_3 = u_2\rho_2$ we obtain

$$[x(\gamma_A + 1)/R(\gamma_B + 1)]^{1/2} = \frac{x+m}{mx+1},$$ (A6)

as our second condition, where R must be understood to mean $R^{critical}$. We now have two

equations, (A1) and (A6) above, for the two "unknowns" x and $R^{critical}$, and the solution

is

$$x = m - 2 = \frac{3 - \gamma_A}{\gamma_A - 1}$$ (A7)

obtained by equating the right-hand-sides of Eqs. (A1) and (A6). With this solution at

hand one can substitute it in either Eq. (A1) or Eq. (A6) to find

$$R^{critical} = \frac{(\gamma_A + 1)(3 - \gamma_A)}{(\gamma_B + 1)(\gamma_A - 1)^3}$$ (A8)

which is Eq. (2).

We illustrate by considering the hydrogen/xenon system. From Table I $\rho_A = 0.0838$

mg/cm^3, $\rho_B = 5.459$ mg/cm^3, $\gamma_A = 1.406$, and $\gamma_B = 1.667$, hence $R \approx 65.14$ and

$R^{critical} \approx 21.49$. Since $R > R^{critical}$ it follows that there is no standing shock, i.e. $W_r > 0$

as can be seen in Fig. 20 where we plot W_r as a function of M_s.

Keeping $\rho_{A,B}$ and γ_B fixed and varying only γ_A (the specific heat ratio of hydrogen)

one can ask for what value of γ_A will $R^{critical}$ equal R. The answer is "γ_A" ≈ 1.282, a

mere 9% lower than the actual $\gamma_{H_2} = 1.406$. This curve is also plotted in Fig. 20 – it

approaches 0 as $M_s \to \infty$. If "γ_A" were even lower, say 1.266, then $R^{critical} \approx 78.3 > R$

and there would be a standing shock and we find $W_r = 0$ at $M_s \approx 10$, as shown by the lowest curve in Fig. 20.

He/air is another system with no standing shock (Fig. 2). If He had a lower γ, say $\gamma_{"He"} = 1.402$ like air, then there *would* be a standing shock at $M_s \approx 3.28$. This sensitivity to γ_A in a shocked A/B system suggest a potential spin-off of the RM instability: The condition $W_r = 0$, i.e. the presence or absence of a standing shock wave as one scans over M_s, can be used as a probe of the equation-of-state, in particular the compressibility of fluid A provided, of course, that γ_B is known. We hope to explore this possibility in condensed matter in the future.

References

[1] A. E. Roberts, "Stability of a steady plane shock," LA report 299, June 1945.

[2] S. P. D'yakov, "Stability of shock waves in inert gases," Zh. Eksp. Teor. Fiz. **27**, 288 (1954).

[3] N. C. Freeman, "A Theory of the Stability of Plane Shock Waves," Proc. R. Soc. London, Ser. A **228**, 341 (1955).

[4] J. G. Wouchuk, C. Huete Ruiz de Lira, and A. L. Velikovich, "Analytical linear theory for the interaction of a planar shock wave with an isotropic turbulent vorticity field," Phys. Rev. E **79**, 066315 (2009).

[5] J. W. Bates, "Theory of the corrugation instability of a piston-driven shock wave," Phys. Rev. E **91**, 013014 (2015).

[6] J. J. Erpenbeck, "Stability of step shocks," Phys. Fluids **5**, 1181 (1962).

[7] Ya. B. Zel'dovich and Yu. P. Raizer, *Physics of Shock Waves and High-Temperature Hydrodynamic Phenomena*, Academic Press (New York), 1967.

[8] R. W. Griffiths, R. J. Sandeman, and H. G. Hornung, "The stability of shock waves in ionizing and dissociating gases," J. Phys. D-Appl. Phys. **9,** 1681 (1976).

[9] C. J. Davie, I. A. Bush, and R. G. Evans, "Stability of shocks relating to the shock ignition inertial fusion energy scheme," Phys. Plasmas **21**, 082701 (2014).

[10] R. D. Richtmyer, "Taylor instability in shock acceleration of compressible fluids," Commun. Pure Appl. Math. **13**, 297 (1960).

[11] E. E. Meshkov, "Instability of the interface of two gases accelerated by a shock wave," Fluid Dyn. **4**, 101 (1969).

[12] K. O. Mikaelian, "Richtmyer-Meshkov instabilities in stratified fluids," Phys. Rev. A **31**, 410 (1985).

[13] J. Hecht, U. Alon, and D. Shvarts, "Potential flow models of Rayleigh–Taylor and Richtmyer–Meshkov bubble fronts," Phys. Fluids **6**, 4019 (1994).

[14] U. Alon, J. Hecht, D. Ofer, and D. Shvarts, "Power laws and similarity of Rayleigh-Taylor and Richtmyer-Meshkov mixing fronts at all density ratios," Phys. Rev. Letters **74**, 534 (1995).

[15] K. O. Mikaelian, "Freeze-out and the effect of compressibility in the Richtmyer–Meshkov instability," Phys. Fluids **6**, 356 (1994).

[16] J. G. Wouchuk, "Growth rate of the linear Richtmyer-Meshkov instability when a shock is reflected," Phys. Rev. E **63**, 056303 (2001).

[17] V. N. Goncharov, "Analytical model of nonlinear, single-mode, classical Rayleigh-Taylor instability at arbitrary Atwood numbers," Phys. Rev. Letters **88**, 134502 (2002).

[18] G. Dimonte and P. Ramaprabhu, "Simulations and model of the nonlinear Richtmyer–Meshkov instability," Phys. Fluids **22**, 014104 (2010).

[19] D. L. Youngs, "Numerical-simulation of mixing by Rayleigh-Taylor and Richtmyer-Meshkov instabilities," Laser & Particle Beams **12**, 725 (1994).

[20] R. M. Baltrusaitis, M. L. Gittings, R. P. Weaver, R. F. Benjamin and J. M. Budzinski, "Simulation of shock-generated instabilities," Phys. Fluids **8**, 2471 (1996).

[21] J. Glimm, M.J. Graham, J. Grove, X.L. Li, T.M. Smith, D. Tan, F. Tangerman, and Q. Zhang, "Front tracking in two and three dimensions," Comp. & Math. App. **35**, 1 (1998).

[22] Q. Zhang and M. J. Graham, "A numerical study of Richtmyer–Meshkov instability driven by cylindrical shocks," Phys. Fluids **10**, 974 (1998).

[23] B. Thornber, D. Drikakis, D. L. Youngs, and R. J. R. Williams, "The influence of initial conditions on turbulent mixing due to Richtmyer–Meshkov instability," J. Fluid Mech. **654**, 99 (2010).

[24] J. M. Budzinski, R. F. Benjamin, and J. W. Jacobs, "Influence of initial conditions on the flow patterns of a shock-accelerated thin fluid layer," Phys. Fluids **6**, 3510 (1994).

[25] M. Vetter and B. Sturtevant, "Experiments on the Richtmyer-Meshkov instability of an air/SF_6 interface," Shock Waves **4**, 247 (1995).

[26] L. Houas and I. Chemouni, "Experimental investigation of Richtmyer-Meshkov instability in shock tube," Phys. Fluids **8**, 614 (1996).

[27] E. Leinov, G. Malamud, Y. Elbaz, L. A. Levin, G. Ben-Dor, D. Shvarts, and O. Sadot, "Experimental and numerical investigation of the Richtmyer-Meshkov instability under re-shock conditions," J. Fluid Mech. **626**, 449 (2009).

[28] J. A. McFarland, J. A. Greenough, and D. Ranjan, "Investigation of the initial perturbation amplitude for the inclined interface Richtmyer–Meshkov instability," Phys. Scripta **T155**, 014014 (2013).

[29] X. Luo, X. Wang, and T. Si, "The Richtmyer-Meshkov instability of a three-dimensional air/SF$_6$ interface with a minimum-surface feature," J. Fluid Mech. **722**, R2 (2013).

[30] G. C. Orlicz, S. Balasubramanian, and K. P. Prestridge, "Incident shock Mach number effects on Richtmyer-Meshkov mixing in a heavy gas layer," Phys. Fluids **25**, 114101 (2013).

[31] C. R. Weber, N. S. Haehn, J. G. Oakley, D. A. Rothamer, and R. Bonazza, "An experimental investigation of the turbulent mixing transition in the Richtmyer-Meshkov instability," J. Fluid Mech. **748**, 457 (2014).

[32] R. L. Holmes, G. Dimonte, B. Fryxell, M. L. Gittings, J. W. Grove, M. Schneider, D. H. Sharp, A. L. Velikovich, R. P. Weaver, and Q. Zhang, "Richtmyer–Meshkov instability growth: experiment, simulation and theory," J. Fluid Mech. **389**, 55 (1999).

[33] M. Brouillette, "The Richtmyer-Meshkov instability," Ann. Rev. Fluid Mech. **34**, 445 (2002).

[34] K. C. Lapworth, "An experimental investigation of the stability of plane shock waves," J. Fluid Mech. **6**, 469 (1959).

[35] M. G. Briscoe and A. A. Kovitz, "Experimental and theoretical study of the stability of plane shock waves reflected normally from perturbed flat walls," J. Fluid Mech. **31**,529 (1968).

[36] A. N. Aleshin, S. G. Zaitsev, and E. V. Lazareva, "Damping of perturbations at a shock front in the presence of a Richtmayer-Meshkov instability," Sov. Tech. Phys. Letters **17**, 493 (1991).

[37] C. Bailie, J. A. McFarland, J. A. Greenough, and D. Ranjan, "Effect of incident shock wave strength on the decay of Richtmyer–Meshkov instability-introduced perturbations in the refracted shock wave," Shock Waves **22**, 511 (2012).

[38] K. O. Mikaelian, "Reshocks, rarefactions, and the generalized Layzer model for hydrodynamic instabilities," Phys. Fluids **21**, 024103 (2009).

[39] A. D. Sakharov, R. M. Zaidel', V. N. Mineev, and A. G. Oleinik, "Experimental investigation of stability of shock waves," Dokl. Akad. Nauk SSSR **159**, 1019 (1964) [Sov. Phys. Dok. **9**, 1091 (1965)].

[40] V. N. Mineev and R. M. Zaidel', "Viscosity of water and mercury under shock load," Zh. Eksp. Teor. Fiz. **54**, 1633 (1968) [Sov. Phys. JETP **27**, 874 (1968)].

[41] G. H. Miller and T. J. Ahrens, "Shock-wave viscosity measurement," Rev. Mod. Phys. **63**, 919 (1991).

[42] E. H. Abramson, "Speculation on measurements of the viscosity of shocked fluid water," Shock Waves **25**, 103 (2015).

[43] K. O. Mikaelian, "Effect of viscosity on Rayleigh-Taylor and Richtmyer-Meshkov instabilities," Phys. Rev. E **47**, 375 (1993).

[44] K. O. Mikaelian, "Shock-induced interface instability in viscous fluids and metals," Phys. Rev. E **87**, 031003 (2013).

[45] C. R. Weber, D. S. Clark, A. W. Cook, L. E. Busby, and H. F. Robey, "Inhibition of turbulence in inertial-confinement-fusion hot spots by viscous dissipation," Phys. Rev. E **89**, 053106 (2014).

[46] D. S. Clark, M. M. Marinak, C. R. Weber, D. C. Eder, S. W. Haan, B. A. Hammel, D. E. Hinkel, O. S. Jones, J. L. Milovich, P. K. Patel, H. F. Robey, J. D. Salmonson, S. M. Sepke, and C. A. Thomas, "Radiation hydrodynamics modeling of the highest compression inertial confinement fusion ignition experiment from the National Ignition Campaign," Phys. Plasmas **22**, 022703 (2015).

[47] R. E. Tipton, in *Megagauss Technology and Pulsed Power Applications*, edited by C. M. Fowler, R. S. Caird, and D. J. Erickson (Plenum, New York, 1987); R. T. Barton, in *Numerical Astrophysics*, edited by J. M. Centrella, J. M. LeBlanc, R. L. Bowers, and J. A. Wheeler (Jones and Bartlett, Boston, 1985).

[48] T. Wang, J-H. Liu, J-S. Bai, Y. Jiang, P. Li, and K. Liu, "Experimental and numerical investigation of inclined air/SF_6 interface instability under shock wave," App. Math. Mech. **33**, 37 (2012).

[49] P. A. Thompson, *Compressible-Fluid Dynamics*, (Maple Press Co., 1984).

[50] M.H. Anderson, B.P. Puranik, J.G. Oakley, P.W. Brooks, and R. Bonazza, "Shock tube investigation of hydrodynamic issues related to inertial confinement fusion," Shock Waves **10**, 377 (2000).

[51] P. B. Puranik, J. G. Oakley, M. H. Anderson, and R. Bonazza, "Experimental study of the Richtmyer-Meshkov instability induced by a Mach 3 shock wave," Shock Waves **13**, 413 (2004).

[52] J. McFarland, D. Reilly, S. Creel, C. McDonald, T. Finn, and D. Ranjan, "Experimental investigation of the inclined interface Richtmyer–Meshkov instability before and after reshock, "Exp. Fluids **55**, 1640 (2014).

[53] K. O. Mikaelian, "Functions $\sin_K x$ and $\cos_K x$," J. Phys. A: Math. Gen. **26**, 1673 (1993).

[54] J. O. Hirschfelder, C. Curtiss, and R. Bird, *Molecular Theory of Gases and Liquids*, (Wiley, N.Y. 1964.)

[55] M. J. Berger and J. Oliger, "Adaptive mesh refinement for hyperbolic partial differential equations," J. Comput. Phys. **53**, 484 (1984).

[56] M.-C. Renoult, P. Carles, S. Ferjani, and C. Rosenblatt, "2D Rayleigh-Taylor instability: Interfacial arc-length vs. deformation amplitude," EPL **101**, 54001 (2013).

[57] V. Kilchyk, R. Nalim, and C. Merkle, "Scaling interface length increase rates in Richtmyer–Meshkov instabilities," J. Fluids Eng. **135**, 031203 (2013).

[58] K. O. Mikaelian, "Boussinesq approximation for Rayleigh-Taylor and Richtmyer-Meshkov instabilities," Phys. Fluids **26**, 054103 (2014).

[59] I. S. Gradshteyn and I. M. Ryzhik, *Table of Integrals, Series, and Products*, (Academic Press, New York, 1980).

[60] H. B. Dwight, *Tables of Integrals and Other Mathematical data*, (Macmillan Company, New York, 1961).

[61] M. Wang, T. Si, and X. Luo, "Generation of polygonal gas interfaces by soap film for Richtmyer–Meshkov instability study," Exp. Fluids **54**, 1427 (2013).

[62] X. Luo, M. Wang, T. Si, and Z. Zhai, "On the interaction of a planar shock with an SF_6 polygon," J. Fluid Mech. **773**, 366 (2015).

[63] L. Erez, O. Sadot, D. Oron, G. Erez, L.A. Levin, D. Shvarts, and G. Ben-Dor, "Study of the membrane effect on turbulent mixing measurements in shock tubes," Shock Waves **10**, 241 (2000).

[64] K. O. Mikaelian, "Richtmyer-Meshkov instability of arbitrary shapes," Phys. Fluids **17**, 034101 (2005).

[65] F. J. Cherne, J. E. Hammerberg, M. J. Andrews, V. Karkhanis, and P. Ramaprabhu, "On shock driven jetting of liquid from non-sinusoidal surfaces into a vacuum," J. App. Phys. **118**, 185901 (2015).

Figure Captions

FIG. 1. Parameters for a shock tube to study the Richtmyer-Meshkov instability. A small perturbation is assumed at the interface between the two fluids A and B, taken to be at rest in the laboratory frame. A shock is traveling down from A towards B and is

characterized by its pressure p_3. The initial fluids are characterized by their densities ρ_A and ρ_B, specific heat ratios γ_A and γ_B, and a common pressure p_0. After the shock strikes the interface two new regions, labeled 1 and 2, are created; regions 0 and 3 are the same as before. The new densities, fluid velocities, and pressures are denoted by ρ_1 and ρ_2, u_1 and u_2, and p_1 and p_2, respectively. The velocities of the transmitted and reflected shocks are denoted by W_t and W_r, respectively. All eight new parameters are determined uniquely by the initial data (see Ref. [15] in which the above figure appears as Fig. 1).

FIG. 2. The velocity W_r of the reflected shock as a function of the Mach number M_s of the incoming shock for 4 A/B systems: N_2/air, air/Xe, H_2/air, and He/air. The sign convention follows Ref. [15]: $W_r > 0$ shock moving up, $W_r < 0$ shock moving down – see Fig. 1.

FIG. 3. Two types of perturbations of the air/CO_2 interface considered in the paper: (a) Sinusoidal with wavelength $\lambda = 13$cm and amplitude $\eta_0 = 3$mm (small) or 3cm (large); (b) Inclined plane with angle $\theta = 60^o$ in a shock tube of width $w = 11.43$cm. The dark circles show the fixed locations of pressure gauges to measure the pressure in the reflected shock which stays ($W_r = 0$) at the location of the original interface.

FIG. 4. Bubble ($\eta > 0$) and spike ($\eta < 0$) evolution for a sinusoidal perturbation shown in Fig. 3(a) with a small initial amplitude of 3mm. The four inviscid/viscous cases described by Eqs. (3a)-(3d) are presented in red, black, blue, and grey curves respectively.

FIG. 5. Same as Fig. 4 with a 10× larger initial amplitude of 3cm.

FIG. 6. Snapshots of the air/CO_2 interface at t=4ms, starting with a large sinusoidal initial amplitude $\eta_0 = 3$ cm, for the 4 cases A, B, C, and D described by Eqs. (3a)-(3d). The time evolution of bubbles and spikes was given in Fig. 5.

FIG. 7. The evolution of bubbles and spikes in the inclined interface with $w = 11.43$cm and $\theta ==60^\circ$. Spikes (bubbles) are defined as the distance between a flat interface and the upper (lower) tip of the inclined surface at $x = 0$ ($x = 11.43$cm) in Fig. 3(b). The colors refer to inviscid/viscous fluids with the same color scheme as in Figs. 4 and 5: red, black, blue, and grey correspond to Eqs. (3a), (3b), (3c), and (3d) respectively.

FIG. 8. Same as Fig. 6 for the inclined interface; t=4ms. Note that the width of each frame here is 11.43cm, while in Fig. 6 the width, comprising of two wavelengths, was 26cm. The letters A, B, C, and D refer to the cases defined by Eqs. (3a)-(3d) respectively.

FIG. 9. The pressure difference Δp in bars between the two fixed points indicated on Fig. 3(a), as a function of time in milliseconds. The points are fixed in space at (x, y)=(0,-6) and (6.5,-6), where the initial interface is given by $y = 3\cos(2\pi x/13)$, all distances in centimeters. The 4 cases A, B, C, and D refer to fluid viscosities given by Eqs. (3a)-(3d). The curves for B, C, and D are shifted down for clarity. At the end of the run, 4ms, the interface is some 180cm below and was shown in Fig. 6 for the 4 cases.

FIG. 10. Snapshots of the density field for case A (upper row) and case D (lower row) at t=1ms (left column) and t=2ms (right column). The 26cm×26cm frames are fixed in

space and cover the region $0 \leq x \leq 26$cm and -30cm$\leq y \leq -4$cm in a coordinate system where the preshock interface is located at $y=0$ and is sinusoidal: $y = \eta_0 \cos 2\pi x / \lambda$ with $\eta_0 = 3$cm and $\lambda = 13$cm – see Fig. 3(a). The pseudo color scale ranges from 3.75 to 3.95 mg/cm^3.

FIG. 11. Same as Fig. 9 for the inclined interface, Fig. 3(b). the points where the pressures are read lie on the shock tube walls, $x=0$ and $x=11.43$cm, and 4cm below the nominal location ($y=0$) of the inclined interface which extends from $y \approx 3.3$cm to $y \approx -3.3$cm.

FIG. 12. Same as Fig. 10 for the inclined interface. The 11.43cm×11.43cm frames are fixed in space and cover the region $0 \leq x \leq 11.43$cm and -15.43cm$\leq y \leq -4$cm. The color scale is the same as in Fig. 10.

FIG. 13. Snapshots of the interface, initially sinusoidal with $\eta_0 = 3$cm, for $L = \infty$ (no reshock, left column) and $L = 50$cm (reshock at 1ms, right column), where L is the length of the test section containing CO_2. This is for the inviscid case A, Eq. (3a).

FIG. 14. Same as Fig. 13 for the viscous case D, Eq. (3d).

FIG. 15. Snapshots of inviscid air/SF_6 and air/CO_2 simulations driven by $M_s = 2.76$ and $M_s = 2.18$ shocks respectively. The downward-moving frames are 26 cm×26 cm and include the interface between the two gases as well as the density fields in pseudo color which ranges from 4 mg/cm^3 to 66 mg/cm^3 for air/SF_6, and from 0.4 mg/cm^3 to 6.6 mg/cm^3 for air/CO_2. The initial configuration is shown in Fig. 3(a) with $\lambda = 13$ cm and $\eta_0 = 1$ cm for both cases.

FIG. 16. 26 cm×26 cm frames fixed in space 4 cm below the initial air/SF_6 interface, recording density fluctuations 0.5, 1.0, 1.5 and 2.0 ms after shock passage. The initial sinusoidal amplitude η_0 was 1cm and the shock had $M_s = M_s^{critical} = 2.76$. The pseudo color ranges from 6.35 mg/cm^3 to 6.65 mg/cm^3.

FIG. 17. The pressure difference Δp in bars between the two fixed points indicated on Fig. 3(a), as a function of time in milliseconds. The red curves refer to air/CO_2 at $M_s = 2.18$, the upper having $\eta_0 = 3$ cm (this is the same as in Fig. 9), the lower $\eta_0 = 1$ cm. The cyan curve also has $\eta_0 = 1$ cm but is for air/SF_6 at $M_s = 2.76$. All inviscid cases. The curves are shifted for clarity.

FIG. 18. Comparison of a standard resolution (2mm×0.46mm) run with a higher resolution (0.5mm×0.23mm). This is for case **A**, inviscid. The Δp from the standard run (red) agrees with the finer run (light blue) which was stopped at 1.12ms. The inset shows the interfaces at that time.

FIG. 19. Excess area parameter $E(t)$ as a function of time for the inviscid case **A** (red) and the viscous case **D** (grey). The upper pair of curves (initial value ≈ 0.40) is for the sinusoidal interface with λ=13cm, η_0=3cm, and the lower pair (initial value ≈ 0.15) is for the inclined interface with $w = 11.43$ cm, θ=60°. Snapshots of the 4 cases at t=4ms were given in Figs. 6(a) and 6(d) (sinusoidal) and in Figs. 8(a) and 8(d) (inclined). Note the logarithmic scale in this figure and compare with the amplitudes shown in Fig. 5 (sinusoidal) and Fig. 7 (inclined). The surface area diagnostic $E(t)$ is much more discriminating than bubble or spike amplitudes.

FIG. 20. Velocity W_r of the reflected shock in the H$_2$/Xe system for 3 values of the hydrogen adiabatic index γ_{H_2}. From Table I the nominal value is γ_{H_2}=1.406 which leads to $R > R^{critical}$ and hence no standing shock is allowed: $W_r > 0$ for all Mach numbers. If γ_{H_2}=1.282 then $R = R^{critical}$ and W_r=0 at $M_s = \infty$. If γ_{H_2} is lower, say 1.266, then $R < R^{critical}$ and W_r=0 at M_s=10.

Table Caption

TABLE I. Densities and specific heat ratios for gases used in the text.

Table I

	H_2	He	N_2	Air	Ar	CO_2	Xe	SF_6
$\rho(Kg/m^3)$	0.0838	0.1664	1.165	1.205	1.662	1.839	5.459	6.146
γ	1.406	1.667	1.401	1.402	1.670	1.297	1.667	1.090

Fig. 1

Fig. 2

48
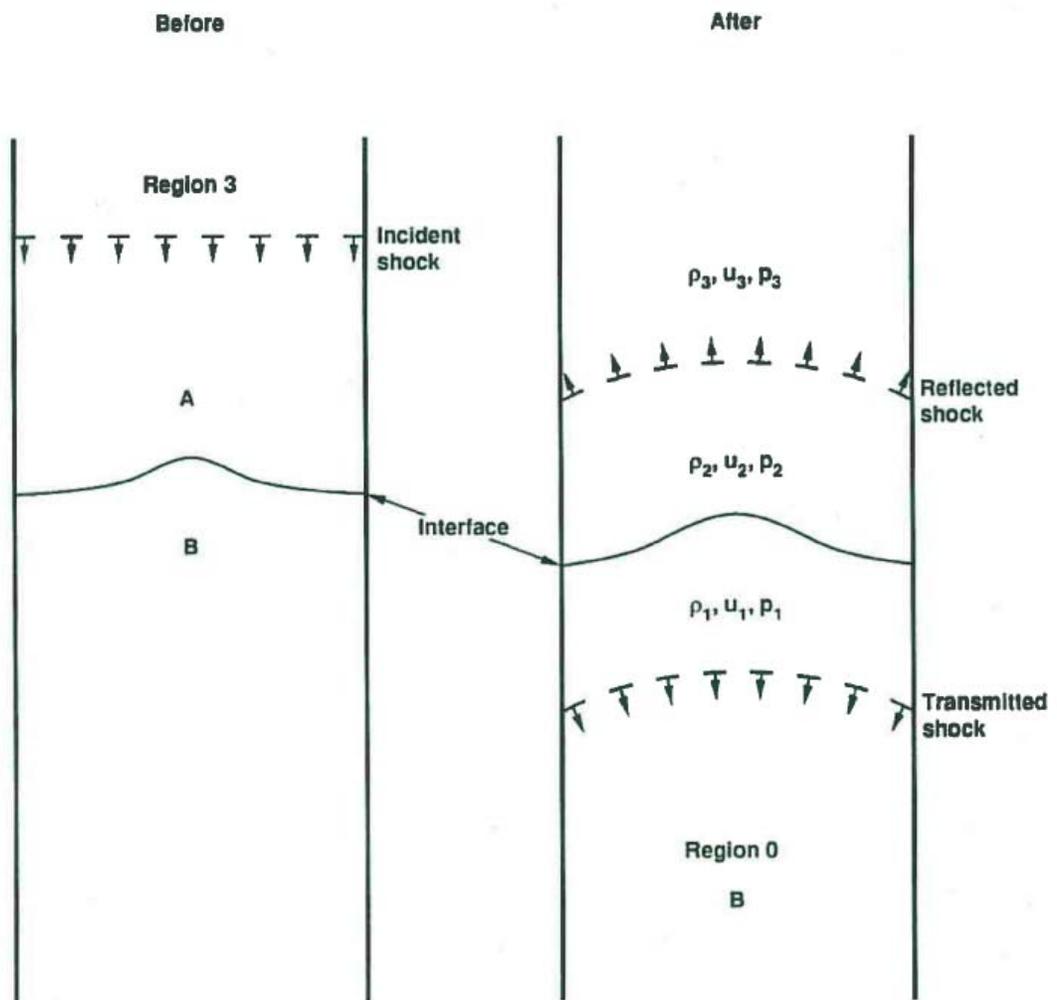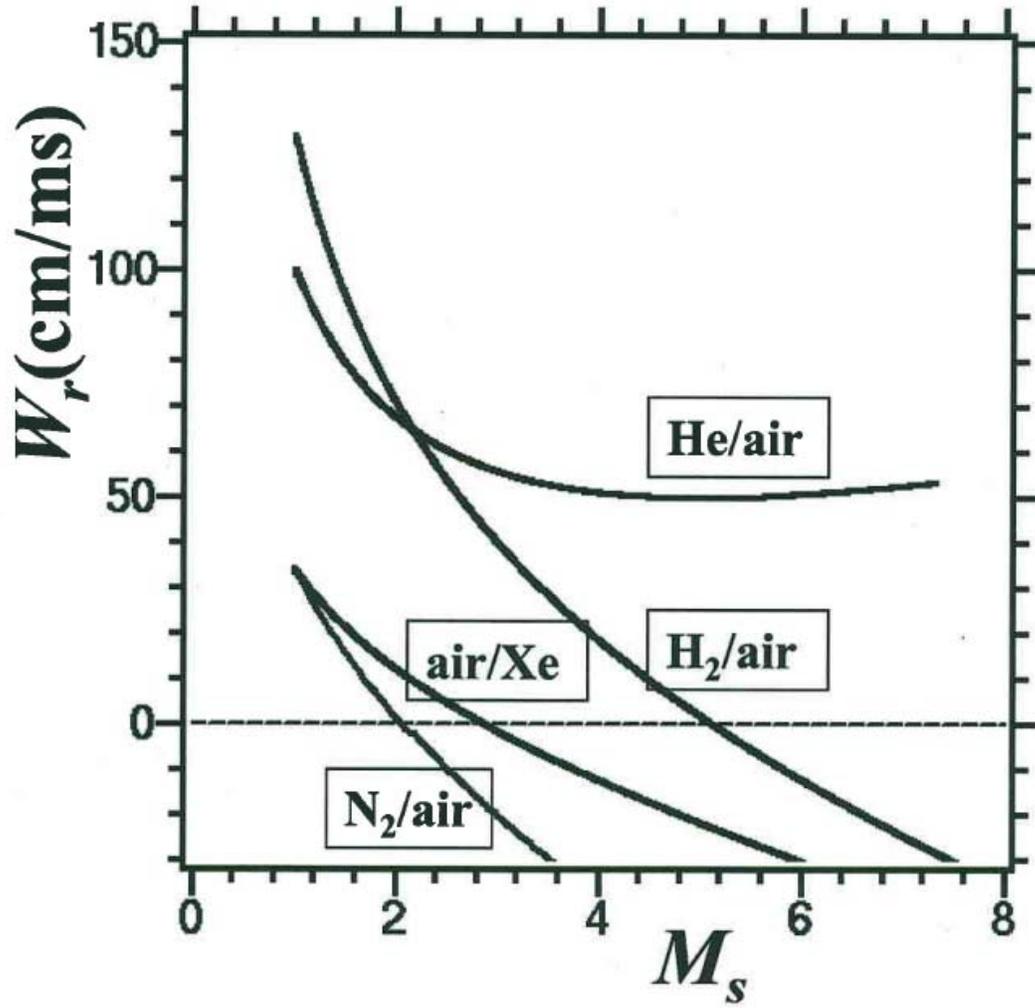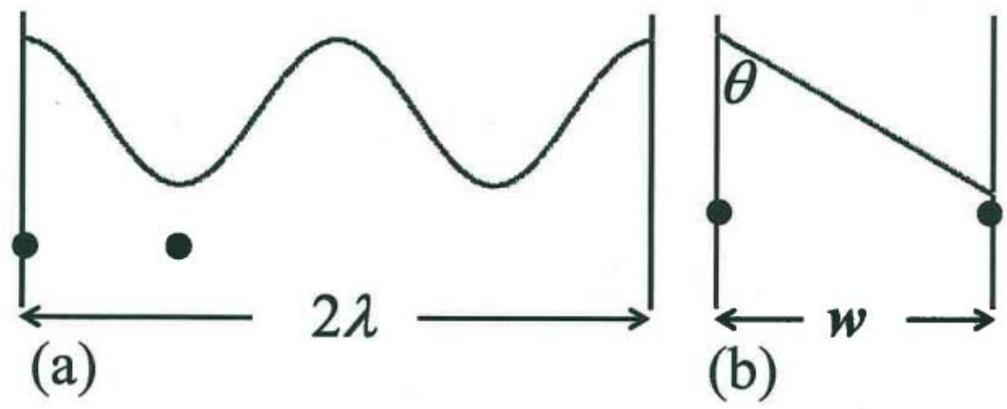
Fig. 3
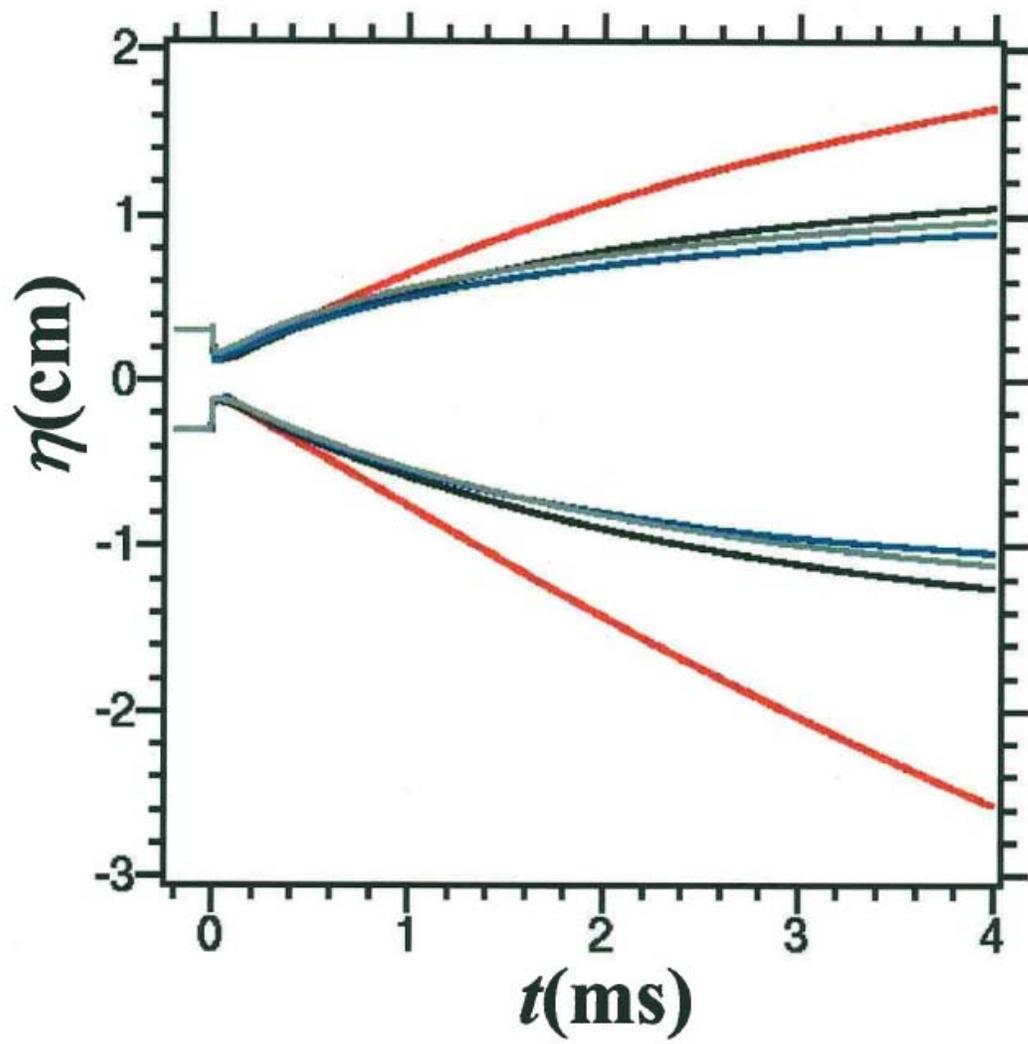
Fig. 4

Fig. 5

Fig. 6

Fig. 7

Fig. 8

Fig. 9

t=1ms t=2ms

Fig. 10

Fig. 11

t=1ms t=2ms

Fig. 12

t (ms)

1.0

1.3

1.6

2.0

L = ∞   *L* = 50 cm

Fig. 13

t (ms)

1.0

1.3

1.6

2.0

$L = \infty$ L=50 cm

Fig. 14

t (ms)

0.5

1.0

1.5

2.0

Air/SF$_6$

M_s=2.76

Air/CO$_2$

M_s=2.18

Fig. 15

t=1.0ms t=1.5ms

t=2.0ms t=2.5ms
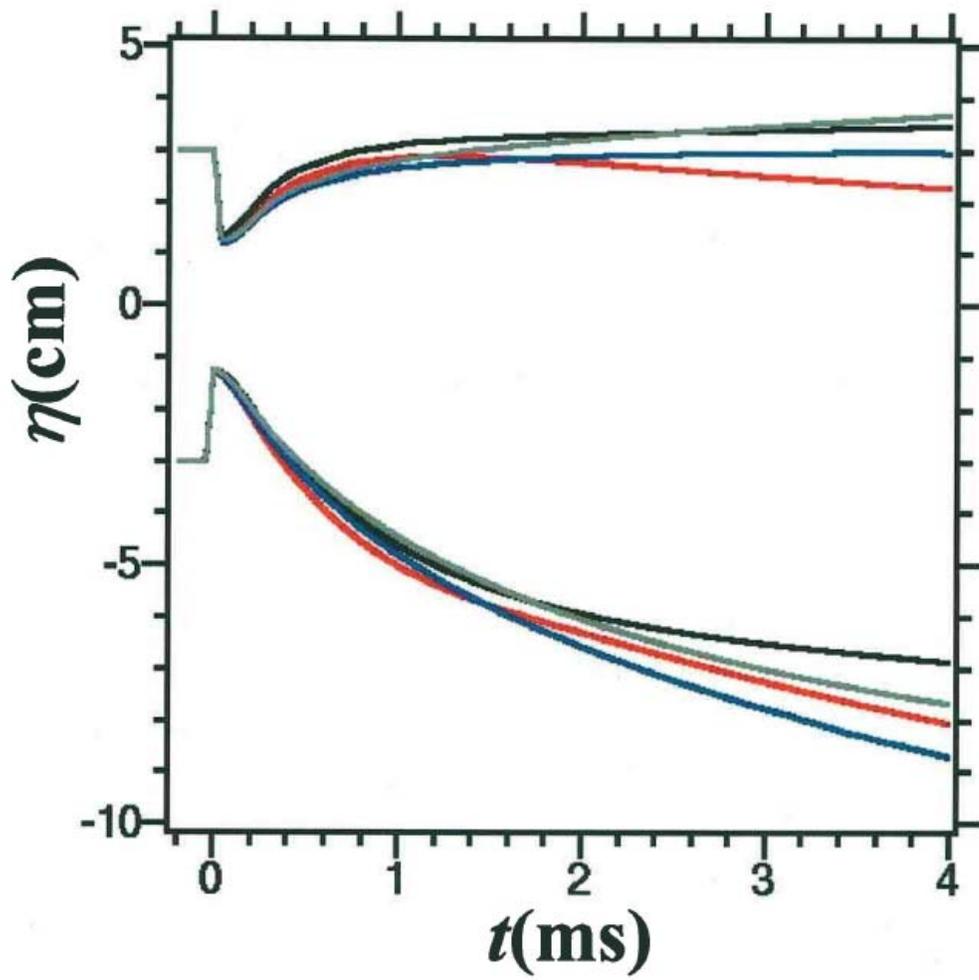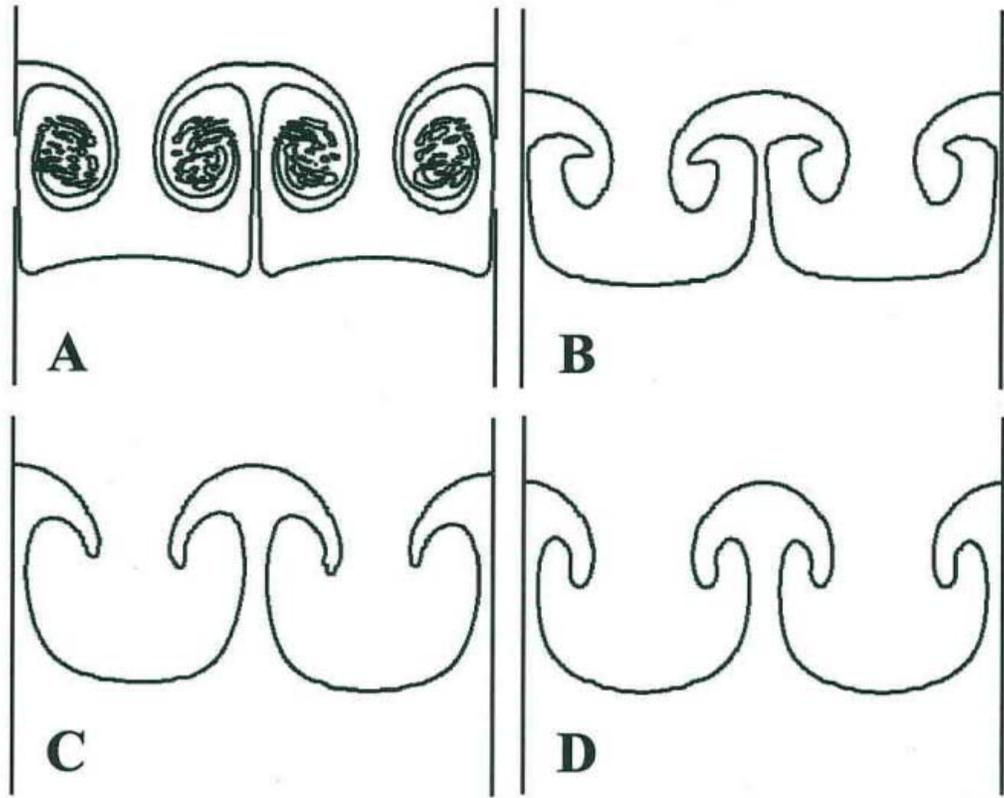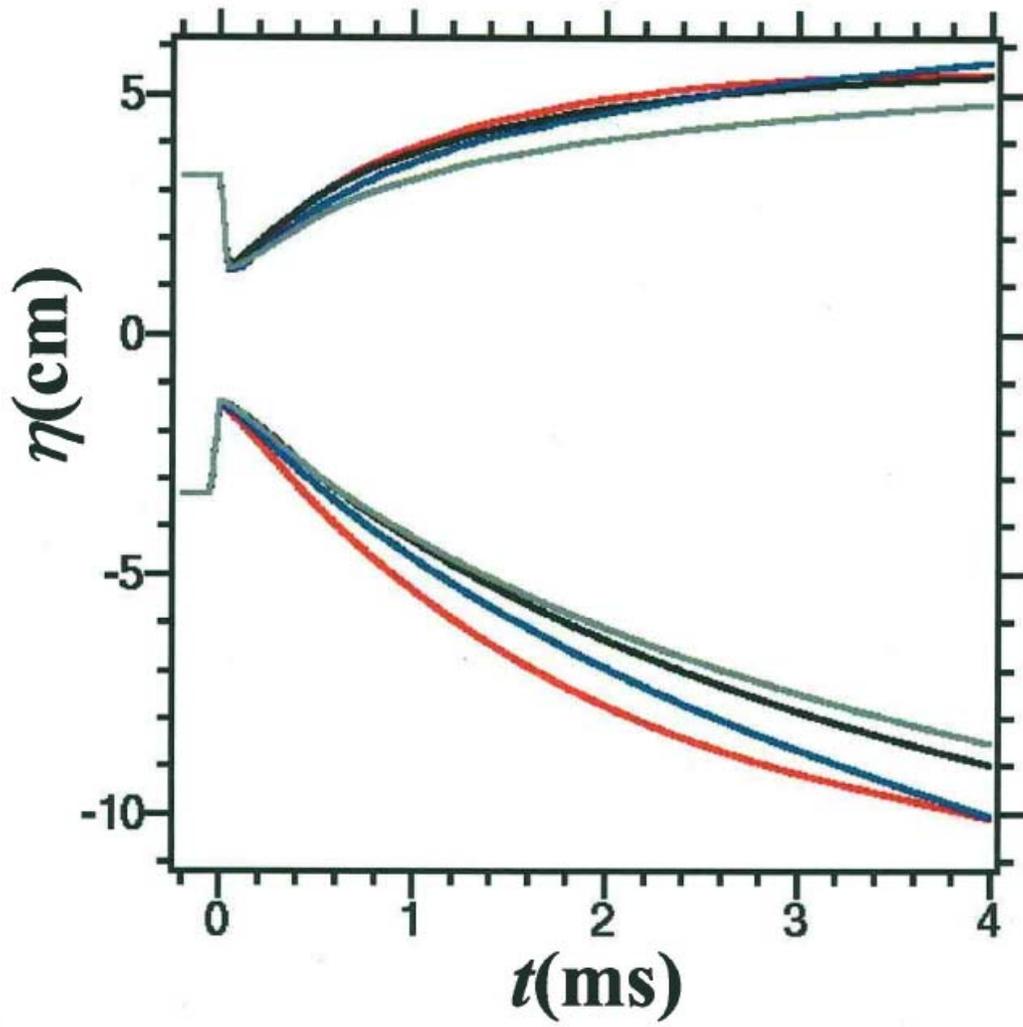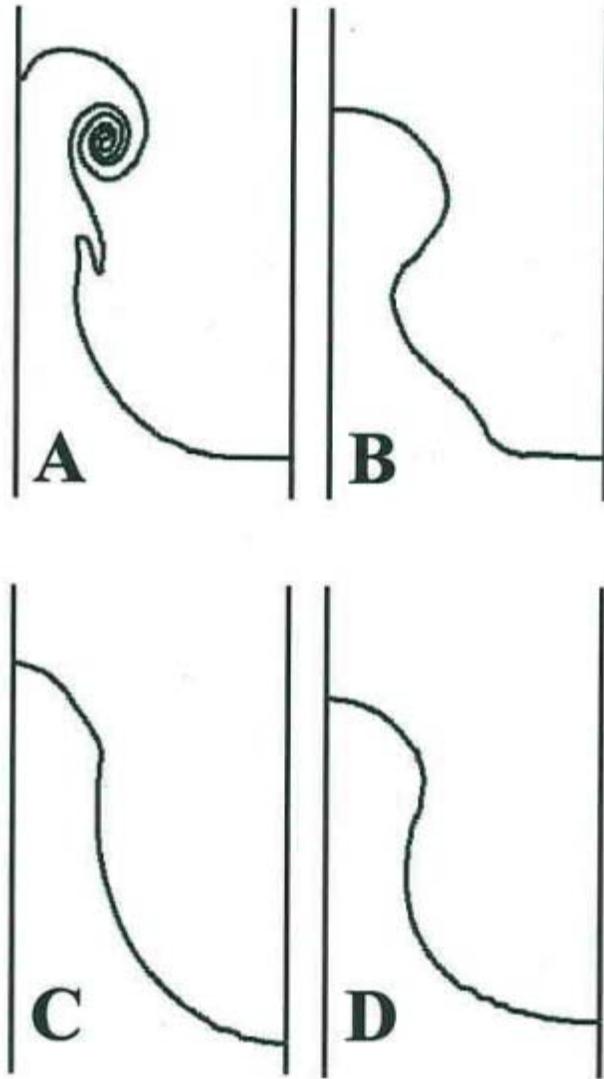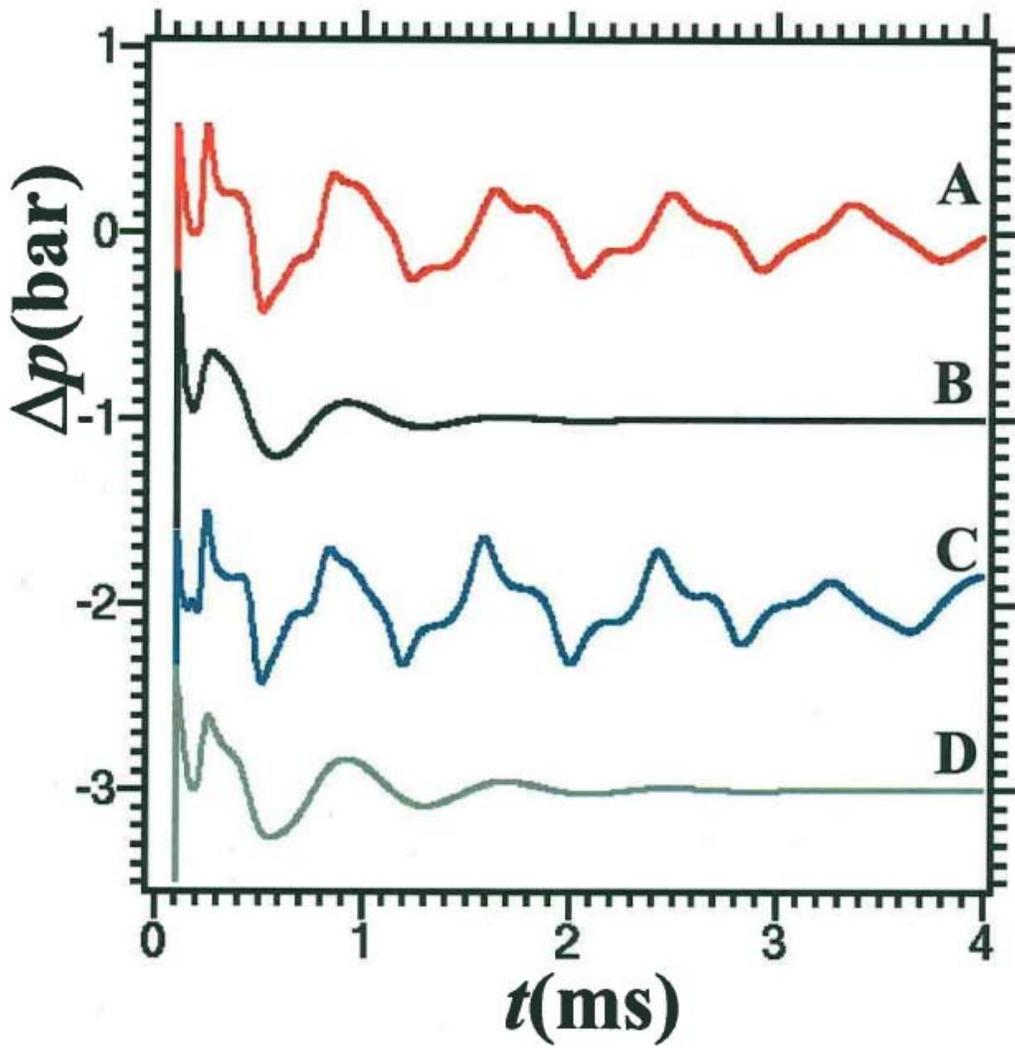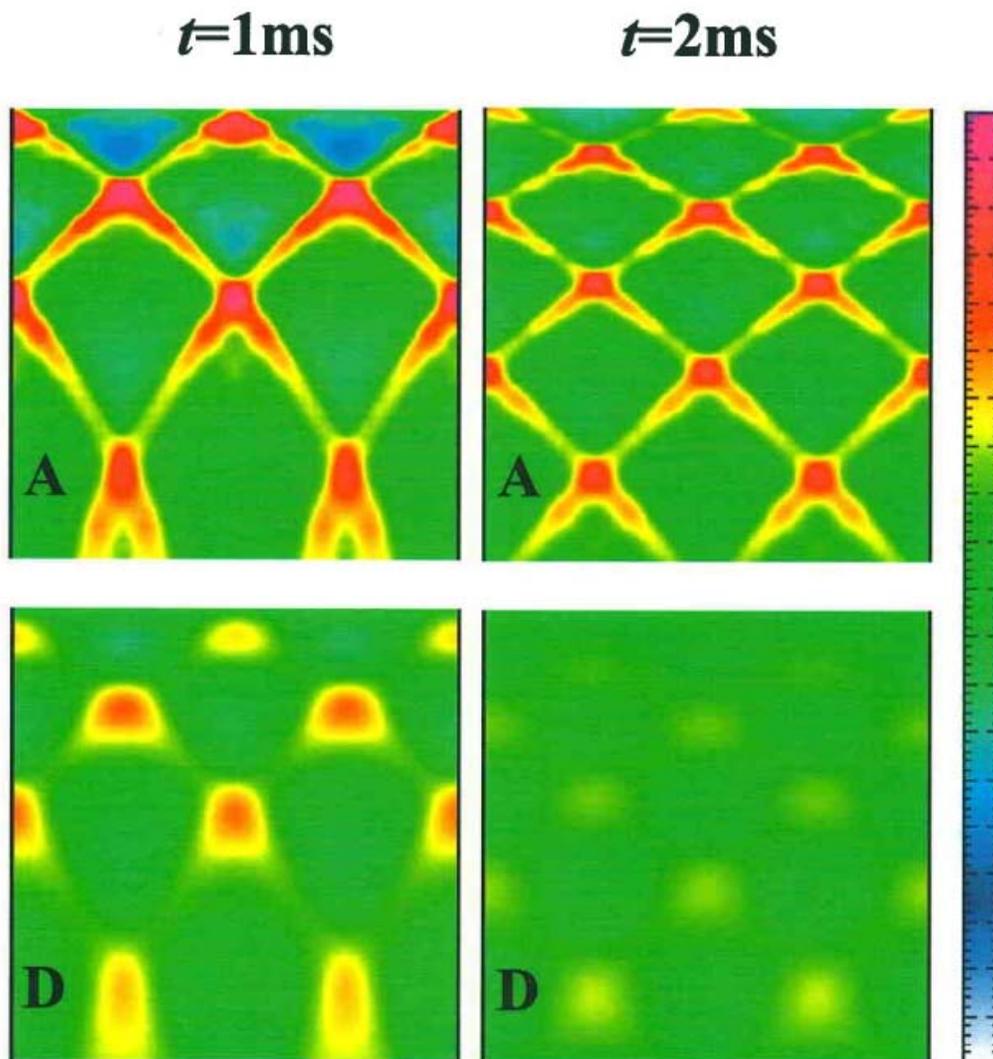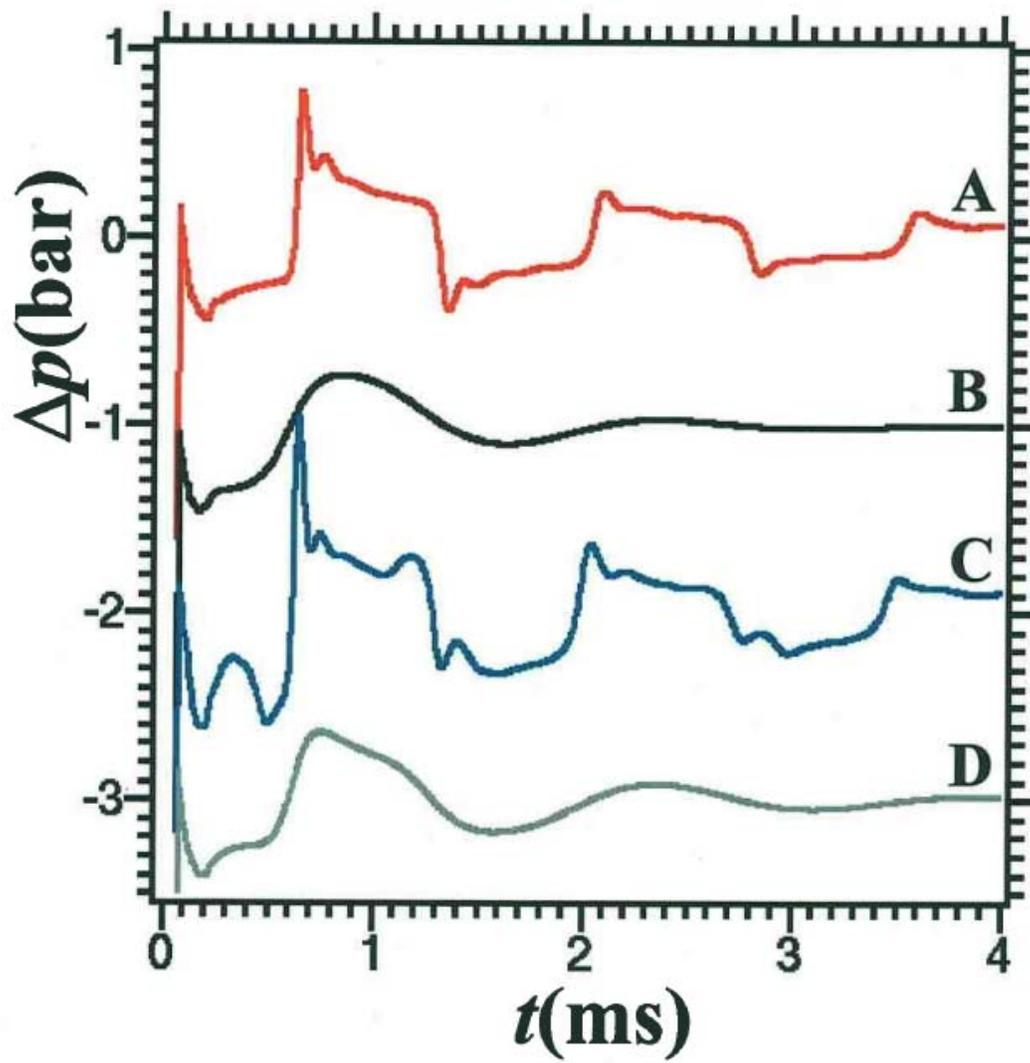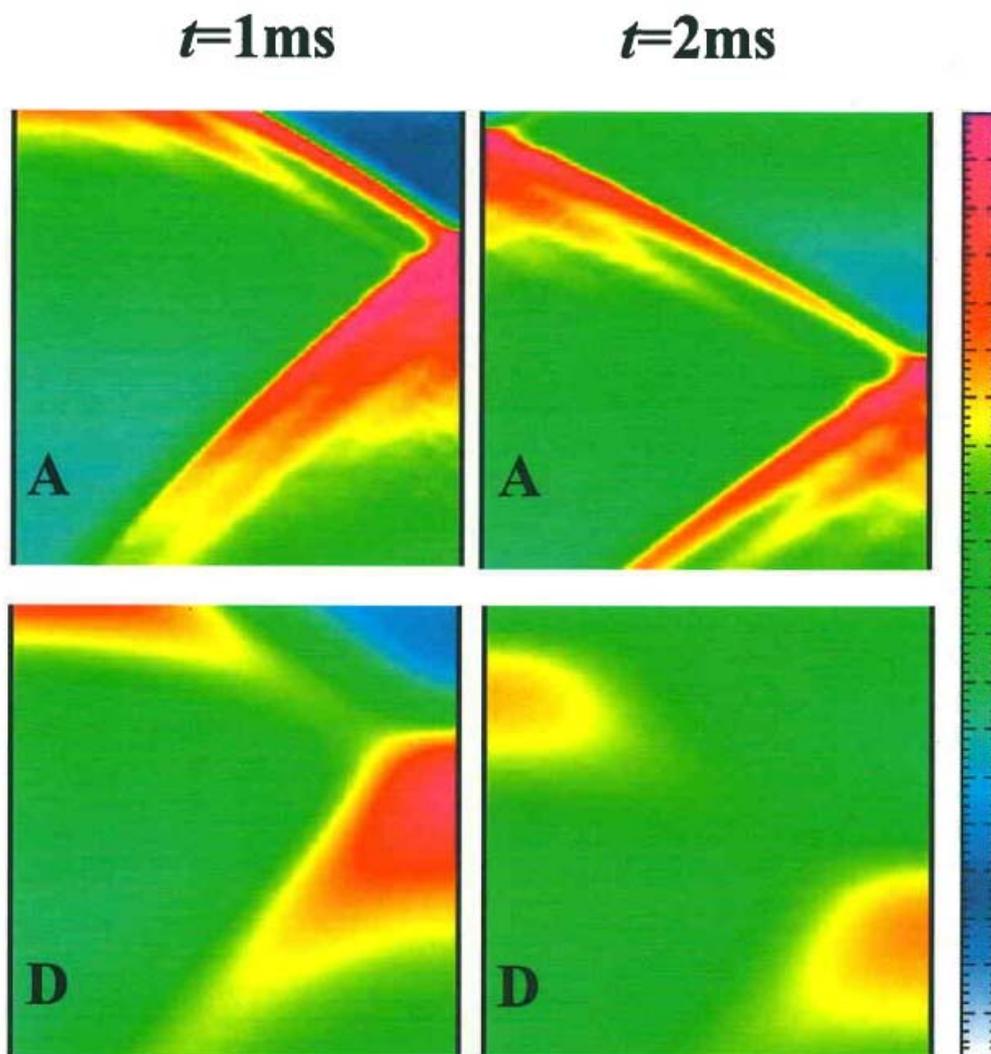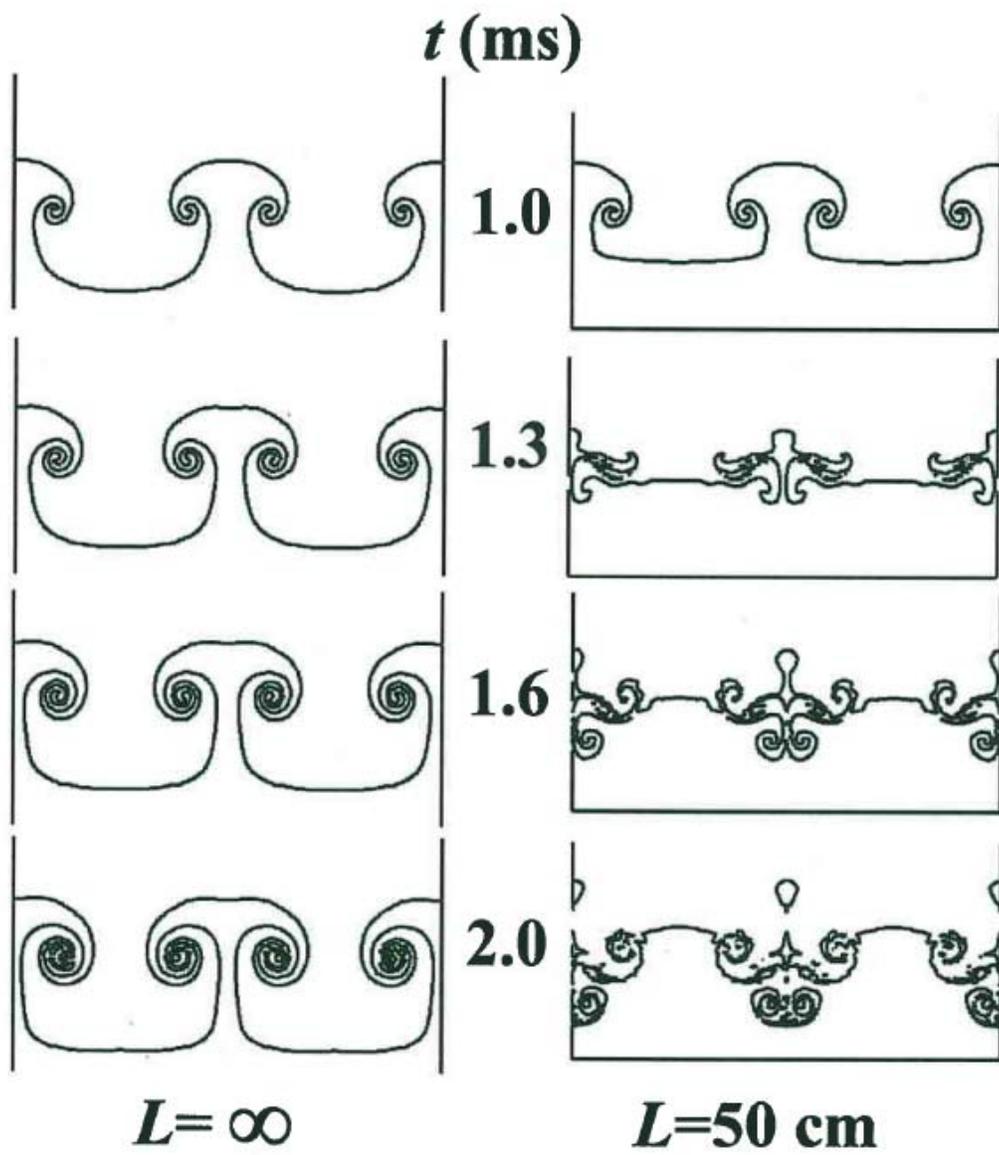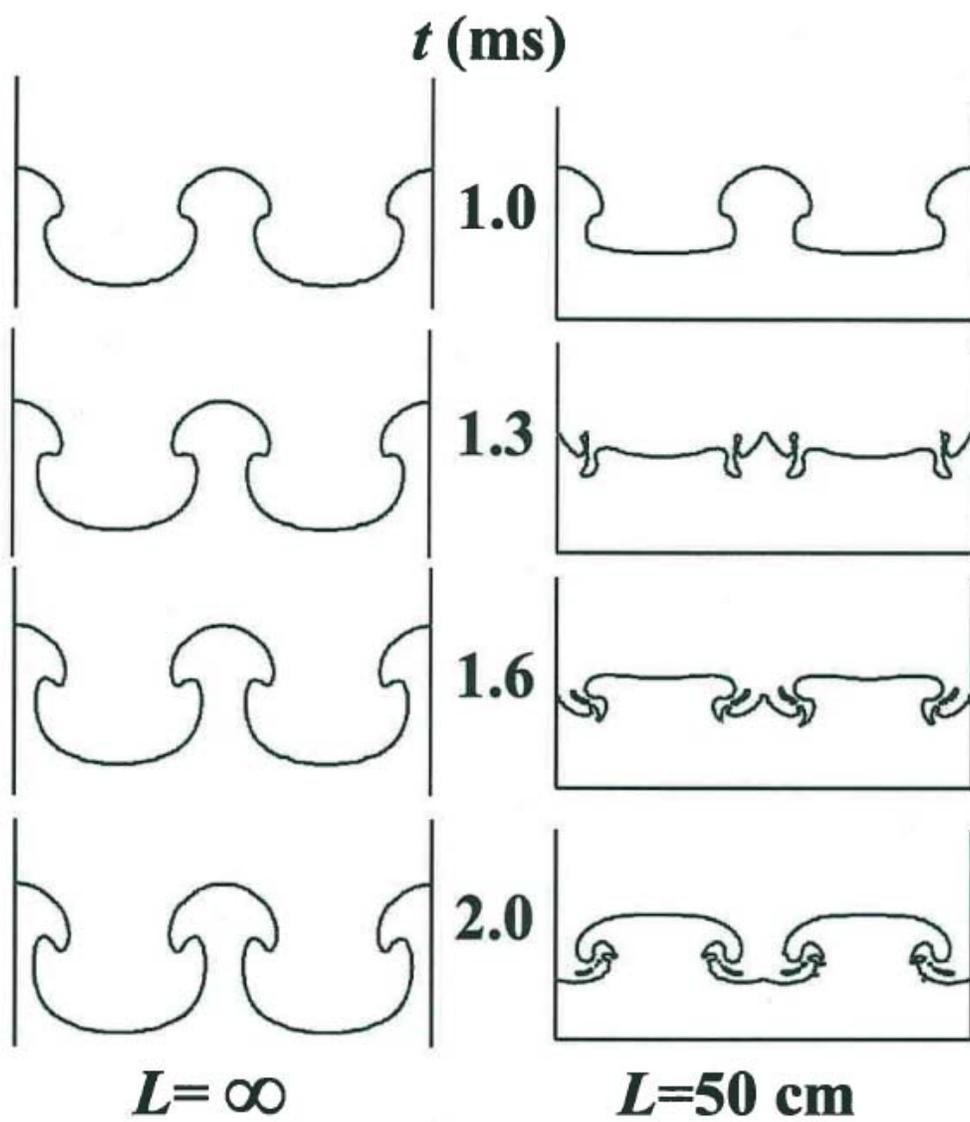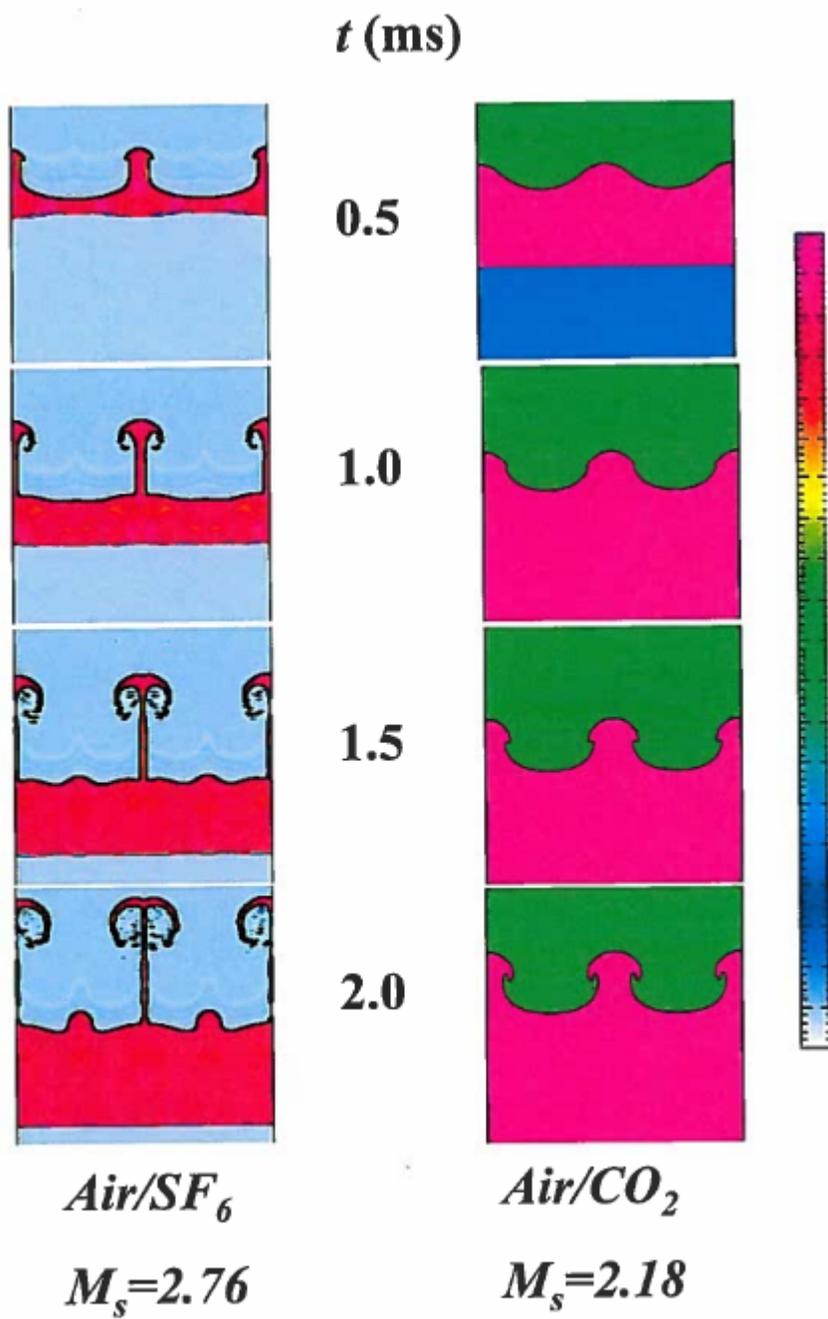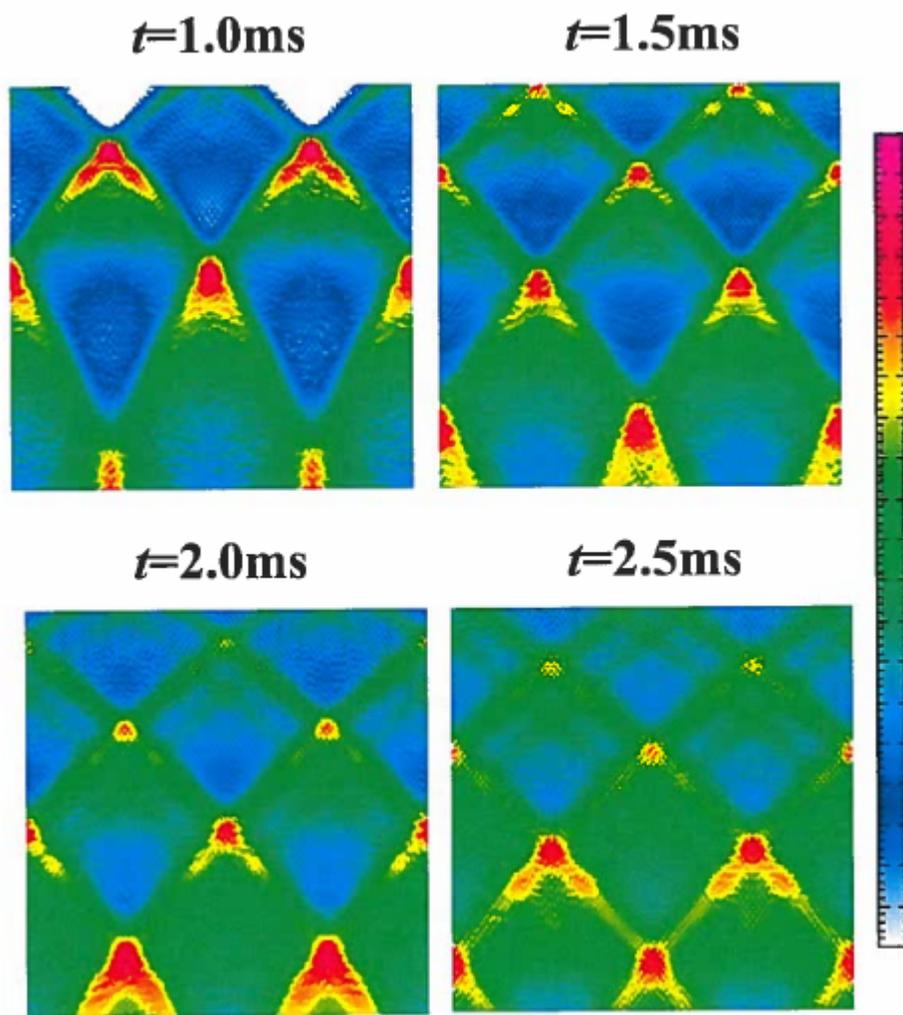
Fig. 16

Fig. 17

Fig. 18

Fig. 19

Fig. 20